

Verification of Eulerian–Eulerian and Eulerian–Lagrangian  
simulations for turbulent fluid–particle flows

Ravi G. Patel<sup>1</sup>, Bo Kong<sup>2\*</sup>, Jesse Capecelatro<sup>3</sup>, Olivier Desjardins<sup>1</sup>, Rodney O. Fox<sup>2,4</sup>

<sup>1</sup>Sibley School of Mechanical and Aerospace Engineering,  
Cornell University, Ithaca, NY 14853, USA

<sup>2,\*</sup>Ames Laboratory – US DOE, Ames, IA 50011-1015, USA

<sup>3</sup>Department of Mechanical Engineering,  
University of Michigan, Ann Arbor, MI, USA

<sup>4</sup>Department of Chemical and Biological Engineering,  
Iowa State University, Ames, IA 50011-2230, USA

August 29, 2017

Accepted Article

## Abstract

We present a verification study of three simulation techniques for fluid–particle flows, including an Euler–Lagrange approach (EL) inspired by Jackson’s seminal work on fluidized particles, a quadrature–based moment method based on the anisotropic Gaussian closure (AG), and the traditional two-fluid model. We perform simulations of two problems: particles in frozen homogeneous isotropic turbulence (HIT) and cluster-induced turbulence (CIT). For verification, we evaluate various techniques for extracting statistics from EL and study the convergence properties of the three methods under grid refinement. The convergence is found to depend on the simulation method and on the problem, with CIT simulations posing fewer difficulties than HIT. Specifically, EL converges under refinement for both HIT and CIT, but statistics exhibit dependence on the post-processing parameters. For CIT, AG produces similar results to EL. For HIT, converging both TFM and AG poses challenges. Overall, extracting converged, parameter-independent Eulerian statistics remains a challenge for all methods.

## Introduction

Fluid–particle flows are ubiquitous in chemical engineering. However, numerical methods that accurately predict such flows are challenging to develop<sup>1</sup>. In fluidized–bed reactors, for example, the large range of scales, from the boundary layers on individual particles to the diameter of the bed, necessitates simulations of flows outside the reach of particle-resolved direct numerical simulation (PR-DNS)<sup>2,3</sup>.

As with single-phase flows, only a coarse-grained approach, via either Reynolds averaging<sup>4</sup>, volume filtering<sup>5</sup>, or multi-phase particle-in-cell<sup>6</sup>, can attempt many simulations of engineering interest. PR-DNS provides useful insights for developing microscale models in these coarse-grained methods<sup>2</sup>. However, knowledge of microscale dynamics is insufficient for accurate simulation of industrial processes. Emergent dynamics, such as the appearance of clusters, play an integral role in the reactor-scale physics. Agrawal et al.<sup>7</sup>, for example, found coarse-grained simulations that fail to account for these dynamics underestimate the settling speed of particles

falling in a gas.

Coarse-grained simulations must incorporate models for these intermediate scales (referred to hereinafter as mesoscale) dynamics. Results from simulations at the mesoscale are needed to develop an understanding of the cluster dynamics and inform models capable of capturing these effects, but even these smaller-scale structures are too large for PR-DNS to resolve. For example, Uhlmann et al.<sup>3</sup> have recently published a study on sedimenting particles in a gas, performing simulations with up to 20,000 particles. While these state-of-the-art PR-DNS simulations are impressive, single clusters may contain many thousands of particles, so we must turn to alternative approaches.

Mesoscale simulation techniques can extend beyond the range possible by PR-DNS. They can simulate the cluster dynamics and inform models for macroscale simulations. Typically, the gas phase is solved via the Navier–Stokes equations, including coupling terms from the effect of the particles. The method used to solve the particle phase distinguishes two classes of mesoscale techniques: Eulerian–Eulerian (EE) and Eulerian–Lagrangian (EL).

EL methods represent particles as discrete points and solve for them using Newton’s Laws. Traditionally, most studies focused on one-way coupled simulations in which the particles do not affect the fluid<sup>8</sup>. However, in denser flows common in industrial processes, the fluid–particle coupling is important and two-way coupled simulations are needed. In fact, for cluster-induced turbulence (CIT)<sup>9</sup>, this coupling is the origin of the clustering phenomenon. In still denser flows, simulations must account for particle–particle collisions. Several studies have investigated this regime using EL methods<sup>10</sup>.

To date, most traditional EL methods are not capable of grid convergence for coupled fluid–particle flows with large particles. Balachandar<sup>11</sup> analyzes the validity of the point-particle assumption. However, for finite-size particles, data must be mapped onto the Eulerian mesh to compute the influence of the particles on the fluid. Garg et al.<sup>12</sup> evaluated various interpolation techniques and showed convergence under mesh refinement is impossible due to increasing statistical error. These authors later<sup>13</sup> proposed replacing the physical particles with computa-

tional ones and adaptively changing the number of particles per grid cell to be within a range. They showed convergence for the momentum coupling in a particle-laden lid-driven cavity flow with this method. However, collisions between the computational particles have to be modeled for dense, collisional flows. The sensitivity to grid resolution observed by Garg et al. can also be alleviated using a volume-filtering approach, introduced by Capecelatro et al.<sup>14</sup> and further refined by Ireland and Desjardins<sup>15</sup>.

EE methods offer a computationally less-expensive alternative to EL methods because they do not have to track individual particles, at the expense of requiring additional modeling. They solve for a reduced, kinetic description for the particle phase. A wide class of techniques have been proposed. Among them, the two-fluid model (TFM), which solves equations for lower order moments of the number density function (NDF), specifically mass, momentum, and granular temperature, remains one of the most popular. However, the main limitation of the TFM is that it is only valid for dense flows in which the frequency of particle-particle collisions is high enough to justify a hydrodynamic description. This assumption is no longer valid for dilute flows with relatively high Stokes numbers<sup>16</sup>, in which particle trajectory crossing (PTC) can be especially prominent. For such flow conditions, quadrature-based moment methods (QBMM) can be used to solve for a poly-kinetic velocity field by establishing a correspondence between a set of moments and a sum of Dirac deltas representation of a NDF via Gaussian quadrature<sup>4</sup>. These techniques not only allow for PTC, but also handle higher-order moments of the NDF than TFM.

Several QBMM methods based on different moment-inversion techniques have been proposed in the literature, including tensor-product<sup>17,18</sup>, CQMOM<sup>19</sup>, multi-Gaussian<sup>20,21</sup>, and anisotropic Gaussian<sup>22</sup>. Among them, the AG closure is the simplest and most robust, and it is computationally inexpensive, and as such it is well-suited for large-scale simulations<sup>23</sup>. Although the AG closure cannot capture the spatial distribution of number density during PTC, it can produce at least the right scale and energetic behavior of PTC<sup>22</sup>. The mesoscale simulations of cluster-induced turbulence (CIT) performed by Kong et al.<sup>23</sup> have demonstrated that AG can produce

results comparable to EL. Therefore, the EE methods considered herein are TFM and AG.

Given the paucity of numerical convergence studies for particle-laden flows, and with the aim of further investigating the differing behaviors of EE and EL methods, this paper presents a detailed verification study for the TFM, AG, and EL approaches from two different perspectives. First, we consider convergence under grid refinement for the three methods. As discussed already, Garg et al.<sup>12</sup> performed grid refinement studies for traditional EL methods, but there have been few studies on grid refinement of volume-filtered EL simulations. Ireland and Desjardins<sup>15</sup> have studied refinement on a single particle falling through fluid. They made modifications that enable volume-filtered EL to recover the Stokes' drag law. Similarly, Gualtieri et al.<sup>24</sup> have introduced a method for choosing the volume-filtering kernel and have performed some tests for convergence. However, neither have not studied refinement of EL simulations of more realistic flows. For EE methods, Agrawal et al.<sup>7</sup> performed simulations of risers using TFM and concluded that a numerical resolution on the order of ten particle diameters is necessary to achieve grid independence. However, the grid-refinement study was limited to two-dimensional domains, and only convergence of the mean slip velocity and granular temperature were reported. Here, we consider behavior of additional methods under mesh refinement, and include the convergence of multiscale statistics.

Second, we investigate post-processing techniques for extracting statistics from EL simulation data. Although volume-filtered EL simulations are robust under grid refinement, as is confirmed in this study, these simulations only provide realizations of the particle state, while we are interested in extracting statistics of the underlying NDF. Subramaniam<sup>25</sup> has established the statistical equivalence between solutions from EL simulations and the Boltzmann equation. Therefore, the relevant statistics can be computed by first estimating the NDF from the Lagrangian particle data. Turbulence modeling will require inferring statistics from simulation results<sup>26</sup>. This presents a challenge for EL specifically because only particle trajectories are computed whereas, in EE, statistical quantities from the NDF are evolved directly. In this paper, we evaluate various techniques for NDF estimation and recovery of statistics for EL.

For verification, we perform simulations of two different fluid–particle flows with moderate Reynolds number particles. First, we study particles in frozen homogeneous isotropic turbulence (HIT). Particles are known to exhibit preferential concentration in such a configuration<sup>27,28</sup>. The parameters chosen for HIT are unphysical in this study. Even so, this flow exhibits interesting clustering dynamics, containing a range of scales with both dilute and dense regions. Few studies have explored convergence and NDF estimation in similar regimes. Additionally, HIT avoids the complexity of two-way coupling and convergence thereof, and therefore it is a good starting point for this study. For detailed studies of particles in HIT see Toschi and Bodenschatz’s recent review<sup>29</sup>. Ultimately, we are interested in fully coupled problems, so as a second configuration, we focus on the denser CIT case wherein two-way coupling is important.

## Governing Equations and Numerical Methods

### Governing Equations

In this section, the governing equations of the fluid and particle phases are briefly presented. The behavior of fluid phase is governed by a continuity equation (1) and a momentum transport equation (2), which are solved in multi-fluid models<sup>30,31</sup>. The continuity equation for the fluid phase is a mass balance,

$$\frac{\partial \rho_f \alpha_f}{\partial t} + \nabla \cdot \rho_f \alpha_f \mathbf{U}_f = 0, \quad (1)$$

where  $\alpha_f$ ,  $\rho_f$ ,  $\mathbf{U}_f$  are fluid-phase volume fraction, density, and velocity, respectively. Note that  $\rho_f$  is assumed to be constant.

The fluid-phase momentum transport equation is derived from momentum balance,

$$\frac{\partial \rho_f \alpha_f \mathbf{U}_f}{\partial t} + \nabla \cdot \rho_f \alpha_f \mathbf{U}_f \otimes \mathbf{U}_f = \nabla \cdot \rho_f \alpha_f \boldsymbol{\sigma}_f - \nabla p_f + \rho_f \alpha_f \mathbf{g} - \frac{\rho_p \alpha_p}{\tau_p} (\mathbf{U}_f - \mathbf{U}_p), \quad (2)$$

where  $\alpha_p$ ,  $\rho_p$ ,  $\mathbf{U}_p$  are the particle-phase volume fraction, density, and velocity, respectively.  $\mathbf{g}$  is the gravity,  $p_f$  and  $\boldsymbol{\sigma}_f$  are the fluid-phase pressure and stress tensor, respectively. The particle-

phase is described by the NDF,  $f(\mathbf{x}, \mathbf{v})$ . The NDF gives the expected number of particles in a region  $\mathbf{x} \in D$  with velocities  $\mathbf{v} \in \Omega$  via integration:  $\int_D \int_\Omega f d\mathbf{v} d\mathbf{x}$ . The NDF is governed by a kinetic equation<sup>23</sup>,

$$\frac{\partial f(\mathbf{x}, \mathbf{v})}{\partial t} + \mathbf{v} \cdot \frac{\partial f(\mathbf{x}, \mathbf{v})}{\partial \mathbf{x}} + \frac{\partial}{\partial \mathbf{v}} \cdot f(\mathbf{x}, \mathbf{v}) \mathbb{A} = \mathbb{C}, \quad (3)$$

where  $\mathbb{A}$  represent acceleration due to gravity and fluid drag and  $\mathbb{C}$  represents particle–particle collisions. In one of the EE approaches presented below, velocity moments up to second order are found from Eq. (3) and the AG closure<sup>22</sup> is invoked to close the higher-order moments. In the other EE approach, the second-order moments are closed using a Chapman–Enskog expansion<sup>32,33</sup>, resulting in a hydrodynamic or TFM.

### Eulerian–Lagrangian Approach

In the EL approach, the fluid phase is solved using the volume-filtering approach introduced by Anderson and Jackson<sup>34</sup>. In this paper, we use the formulation developed by Capecelatro and Desjardins<sup>14</sup>. The volume-filtering operation is defined as a convolution with a kernel,  $\mathcal{H}(|\mathbf{x}|)$ , over the volume occupied by the fluid,  $\mathcal{V}_f$ , giving

$$\alpha_f \bar{\mathbf{a}} = \mathcal{H} \star \mathbf{a} = \int_{\mathcal{V}_f} \mathbf{a}(\mathbf{y}) \mathcal{H}(|\mathbf{x} - \mathbf{y}|) d\mathbf{y}, \quad (4)$$

where  $\alpha_f$  is the fluid volume fraction and  $\mathbf{a}$  is the fluid quantity to be filtered. For a constant density fluid, filtering the mass conservation and Navier–Stokes equations yields

$$\begin{aligned} \frac{\partial}{\partial t} (\alpha_f \rho_f) + \nabla \cdot (\alpha_f \rho_f \bar{\mathbf{U}}_f) &= 0, \\ \frac{\partial}{\partial t} (\alpha_f \rho_f \bar{\mathbf{U}}_f) + \nabla \cdot (\alpha_f \rho_f \bar{\mathbf{U}}_f \otimes \bar{\mathbf{U}}_f) &= \nabla \cdot \bar{\boldsymbol{\tau}} + \alpha_f \rho_f \mathbf{g} - \mathcal{F}_U + \mathcal{F}_\mu - \mathcal{F}^{\text{inter}}, \end{aligned} \quad (5)$$

where  $\bar{\boldsymbol{\tau}} = -p_f \mathbf{I} + \mu_f \left[ \nabla \bar{\mathbf{U}}_f + \nabla \bar{\mathbf{U}}_f^T - \frac{2}{3} (\nabla \cdot \bar{\mathbf{U}}_f) \mathbf{I} \right]$ . For CIT, Capecelatro et al.<sup>14</sup> demonstrated the sub-grid stress,  $\mathcal{F}_U$ , contributes insignificantly to the momentum balance so it is neglected in this study. Following Capecelatro et al.<sup>14</sup>, we use Gibilaro’s model<sup>35</sup> for the residual viscous

stress,  $\mathcal{F}_\mu$ .

The interphase exchange term,  $\mathcal{F}^{\text{inter}}$ , can be decomposed into resolved and unresolved components as

$$\mathcal{F}^{\text{inter}} = \mathcal{F}_{\text{residual}}^{\text{inter}} + \mathcal{F}_{\text{resolved}}^{\text{inter}}, \quad (6)$$

where the resolved component is approximated as

$$\mathcal{F}_{\text{resolved}}^{\text{inter}} = \sum \mathcal{H} \star \mathbf{F}_{\text{resolved}}^{(i)} \approx V_p \sum \mathcal{H} \star \nabla \cdot \bar{\tau}|_{\mathbf{x}_p^{(i)}} = (1 - \alpha_f) \nabla \cdot \bar{\tau}. \quad (7)$$

In the previous equation,  $\cdot|_{\mathbf{x}_p^{(i)}}$  indicates that the fluid quantities are evaluated at the location of particle  $i$ . The residual component is computed as

$$\mathcal{F}_{\text{resolved}}^{\text{inter}} = \sum \mathcal{H} \star \mathbf{F}_{\text{residual}}^{(i)}, \quad (8)$$

where  $\mathbf{F}_{\text{residual}}^{(i)}$  is the residual force from particle  $i$  and must be modeled.

The state of the  $i$ th particle,  $\{\mathbf{x}_p^{(i)}, \mathbf{v}_p^{(i)}\}$ , is found via integration of Newton's Laws,

$$\begin{aligned} \frac{d\mathbf{x}_p^{(i)}}{dt} &= \mathbf{v}_p^{(i)}, \\ m_p \frac{d\mathbf{v}_p^{(i)}}{dt} &= \mathbf{F}^{(i)} = \mathbf{F}_{\text{resolved}}^{(i)} + \mathbf{F}_{\text{residual}}^{(i)} + m_p \mathbf{g} + \mathcal{C}, \end{aligned} \quad (9)$$

where  $\mathbf{g}$  and  $\mathcal{C}$  are the contributions from gravity and particle–particle collisions. In this work, we consider particles of small Reynolds number,  $Re_p \ll 1$ , and of high density,  $\rho_p \gg \rho_f$ . Therefore, we use a Stokes drag law to model the residual portion of the exchange term,

$$\mathbf{F}_{\text{residual}}^{(i)} = \frac{m_p \tilde{\alpha}_f|_{\mathbf{x}_p^{(i)}}}{\tau_p} \left( \tilde{\mathbf{U}}_f|_{\mathbf{x}_p^{(i)}} - \mathbf{v}_p^{(i)} \right). \quad (10)$$

For accurate simulation of flows in which fluid–particle coupling plays a significant role, Ireland and Desjardins<sup>15</sup> demonstrated that the fluid volume fraction,  $\tilde{\alpha}_f|_{\mathbf{x}_p^{(i)}}$ , and velocity,  $\tilde{\mathbf{U}}_f|_{\mathbf{x}_p^{(i)}}$ , must represent *undisturbed* quantities, i.e., the quantities if the particle  $i$  were not



present. We use the approach introduced by Ireland and Desjardins<sup>15</sup> for estimating these quantities from the filtered fluid volume fraction and velocity. This correction is necessary to ensure the Stokes settling speed is recovered in well-resolved simulations of a single particle falling in fluid.

### Statistics via Number-Density Estimation

The simplest techniques for estimating the NDF from the particle field are based on projecting the particle information onto a Eulerian mesh. The NDFs found from these histogram density estimation techniques depend on the mesh spacing, which cannot be specified uniquely as discussed by Garg et al.<sup>12</sup>. Instead, Capecelatro et al.<sup>14</sup> used a kernel density estimation technique. A realization of the particle state can be described as

$$\hat{f}(\mathbf{x}, \mathbf{v}) = \sum \delta(\mathbf{x} - \mathbf{x}_p^{(i)}) \delta(\mathbf{v} - \mathbf{v}_p^{(i)}). \quad (11)$$

The NDF can be approximated by convolution of  $\hat{f}$  with a normalized kernel  $G_h$  with bandwidth  $h$  over the simulation domain:

$$f(\mathbf{x}, \mathbf{v}) \approx G_h(|\mathbf{x}|) * \hat{f}(\mathbf{x}, \mathbf{v}) = \sum G_h(|\mathbf{x} - \mathbf{x}_p^{(i)}|) \delta(\mathbf{v} - \mathbf{v}_p^{(i)}) \quad (12)$$

Moments of this NDF give the equivalent Eulerian quantities in EE simulations. For example, the particle volume fraction, Eulerian particle velocity, and granular temperature are given by

$$\alpha_p = V_p \int f \mathbf{d}\mathbf{v} = V_p \sum G_h(|\mathbf{x} - \mathbf{x}_p^{(i)}|), \quad (13)$$

$$\alpha_p \mathbf{U}_p = V_p \int \mathbf{v} f \mathbf{d}\mathbf{v} = V_p \sum G_h(|\mathbf{x} - \mathbf{x}_p^{(i)}|) \mathbf{v}_p^{(i)}, \quad \text{and} \quad (14)$$

$$\alpha_p \Theta_p = \frac{V_p}{3} \int |\mathbf{v} - \mathbf{U}_p|^2 f \mathbf{d}\mathbf{v} = \frac{V_p}{3} \sum G_h(|\mathbf{x} - \mathbf{x}_p^{(i)}|) |\mathbf{v}_p^{(i)} - \mathbf{U}_p|^2. \quad (15)$$

However, the selection of the bandwidth,  $h$ , may significantly affect results from EL simulations.

Capecelatro et al.<sup>9</sup> have previously studied the sensitivity of the selection of filter  $G_h$  on statistics from CIT. They also proposed an adaptive filter width, defined recursively, that appears to reduce the parameter sensitivity, using

$$h^n(\mathbf{x}) = \left( \frac{\mathcal{N}_p d_p^3}{\alpha_p^{n-1}(\mathbf{x})} \right)^{1/3}, \quad (16)$$

where  $h^0$  is an initially fixed filter width. This filter is built to sample approximately  $\mathcal{N}_p$  particles.

Voronoi tessellation is an alternative technique for density estimation that has recently received attention in both experimental<sup>36,37</sup> and computational<sup>3</sup> studies of particle-laden flows. In this technique, the Voronoi tessellation of the set of particle locations defines an unstructured Eulerian mesh. The volume fraction of each cell is set according to

$$\alpha_p(\mathbf{x}) = \frac{V_p}{V_{\text{cell}^{(i)}}} \text{ for } \mathbf{x} \in \text{cell}^{(i)}. \quad (17)$$

Here, we chose the Eulerian particle velocity for each cell to be defined by

$$\mathbf{U}_p(\mathbf{x}) = \frac{1}{n^{(i)}} \sum_j \mathbf{v}_p^{(j)} \text{ for } \mathbf{x} \in \text{cell}^{(i)}. \quad (18)$$

where  $n^{(i)}$  is the number of cells adjacent to cell  $i$  and  $\mathbf{v}_p^{(j)}$  is the velocity of the particle in cell  $j$  adjacent to cell  $i$ .

We are particularly interested in computing the variance in volume fraction and the average granular temperature from simulations because they have important modeling implications<sup>4,38</sup>. Using the ensemble average,  $\langle \cdot \rangle$ , the volume fraction variance is defined as

$$\langle \alpha_p'^2 \rangle = \langle (\alpha_p - \langle \alpha_p \rangle)^2 \rangle = \langle \alpha_p^2 \rangle - \langle \alpha_p \rangle^2. \quad (19)$$

From the Eulerian particle velocity field, the velocity of particle  $i$  can be separated into correlated

and uncorrelated components as

$$\mathbf{v}_p^{(i)} = \mathbf{U}_p|_{\mathbf{x}_p^{(i)}} + \delta\mathbf{v}_p^{(i)}. \quad (20)$$

Following Fox et al.<sup>4</sup>, particle-phase averaging of a quantity  $\phi$  is defined as  $\langle\phi\rangle_p = \frac{\langle\alpha_p\phi\rangle}{\langle\phi\rangle}$ . The average granular temperature is then computed as

$$\langle\Theta_p\rangle_p = \frac{1}{3} \langle\delta\mathbf{v}_p \cdot \delta\mathbf{v}_p\rangle. \quad (21)$$

As shown above, the granular temperature is approximated for EL as the velocity fluctuation variance below a certain scale, depending on the density estimation technique used. We hope to recover the true granular temperature, the variance from the underlying number density function, with a careful selection of technique and parameters for estimating the NDF. Figure 1 provides a visual comparison of the histogram, kernel, and Voronoi density estimation techniques.

Note that the granular temperature is a separate quantity from the total velocity fluctuation energy. The total fluctuation energy contains contributions from granular temperature and the particle turbulent kinetic energy, i.e.,

$$\begin{aligned} \kappa_p &= k_p + \frac{3}{2} \langle\Theta_p\rangle_p, \\ \text{where } \kappa_p &= \frac{1}{2} \langle|\mathbf{v}'|^2\rangle \text{ and } k_p = \frac{1}{2} \left\langle \left| \mathbf{U}_p - \langle\mathbf{U}_p\rangle_p \right|^2 \right\rangle_p. \end{aligned} \quad (22)$$

Fox et al.<sup>4,26</sup> discuss the importance of this distinction for modeling. In this study, we consider fixed and adaptive kernel density estimation and the Voronoi tessellation techniques for computing various statistics from the simulation data. Simulations are performed in NGA, a multiphase flow solver introduced by Desjardins et al.<sup>39</sup>. We use the Voro++ library<sup>40</sup> to perform the Voronoi tessellations.

## Eulerian–Eulerian Approaches

The transport equations for three lower-order moments of particle velocity NDF, i.e., particle mass, momentum, and granular energy tensor, are given by

$$\frac{\partial \rho_p \alpha_p}{\partial t} + \nabla \cdot \rho_p \alpha_p \mathbf{U}_p = 0, \quad (23)$$

$$\frac{\partial \rho_p \alpha_p \mathbf{U}_p}{\partial t} + \nabla \cdot \rho_p \alpha_p (\mathbf{U}_p \otimes \mathbf{U}_p + \mathbf{P}_p + \mathbf{G}_p) = \rho_p \alpha_p \mathbf{g} + \frac{\rho_p \alpha_p}{\tau_p} (\mathbf{U}_f - \mathbf{U}_p), \quad \text{and} \quad (24)$$

$$\begin{aligned} \frac{\partial \rho_p \alpha_p \mathbf{P}_p}{\partial t} + \nabla \cdot \rho_p \alpha_p (\mathbf{U}_p \otimes \mathbf{P}_p + \mathbf{Q}_p + \mathbf{H}_p) = \\ - \rho_p \alpha_p [\mathbf{P}_p \cdot \nabla \mathbf{U}_p + (\mathbf{P}_p \cdot \nabla \mathbf{U}_p)^T] - \rho_p \alpha_p \frac{2}{\tau_p} \mathbf{P}_p + \rho_p \alpha_p \frac{2}{\tau_c} (\Delta^* - \mathbf{P}_p), \end{aligned} \quad (25)$$

where  $\mathbf{P}_p$  is the particle pressure tensor,  $\mathbf{Q}_p$  is the kinetic-flux tensor due to third-order central moments,  $\mathbf{G}_p$  and  $\mathbf{H}_p$  is the collisional flux tensor for particle-phase momentum and granular energy tensor, respectively. In Eq. (25), a linearized Bhatnagar–Gross–Krook (BGK) inelastic collision model<sup>41</sup> is used to account for the collisional dissipation of  $\mathbf{P}_p$ , in which  $\tau_c = d_p / (6\alpha_p g_0 \sqrt{\Theta_p / \pi})$  and  $\Delta^* = \eta^2 \Theta_p \mathbf{I} + (1 - \eta)^2 \mathbf{P}_p$ .

In the first EE approach, the particle NDF is assumed to follow an anisotropic Gaussian distribution, and a three-dimensional Gauss–Hermite quadrature is used to close the spatial transport of moments<sup>22,23</sup>, i.e.,

$$f(\mathbf{v}) = \frac{\alpha_p}{(2\pi|\mathbf{P}_p|)^{3/2}} \exp \left[ -\frac{1}{2} (\mathbf{v} - \mathbf{U}_p) \cdot \mathbf{P}_p^{-1} \cdot (\mathbf{v} - \mathbf{U}_p) \right]. \quad (26)$$

In this approach, the collisional flux for momentum,  $\mathbf{G}_p$ , is modeled as,  $\mathbf{G}_p = \frac{4}{5} \eta \alpha_p g_0 (3\Theta_p \mathbf{I} + 2\mathbf{P}_p)$ , using the Enskog–Boltzmann kinetic theory<sup>42</sup>, where  $\eta = \frac{1}{2}(1 + e)$ ,  $e$  is the particle collision restitution coefficient. The particle radial distribution function  $g_0$  can be modeled as,  $g_0 = (1 - \frac{1}{2}\alpha_p) / (1 - \alpha_p)^{3/4}$ . The collisional flux for pressure tensor,  $\mathbf{H}_p$ , is ignored. More details on the numerical method used to solve the AG model can be found elsewhere<sup>23</sup>.

In the second EE approach, a hydrodynamic description (TFM) of particle dynamics is used, so the particle-pressure tensor is decomposed into its isotropic and anisotropic components<sup>16</sup>:  $\mathbf{P}_p = \Theta_p \mathbf{I} - \boldsymbol{\sigma}_p$ . The kinetic contribution to the granular stress tensor is closed with a gradient-viscosity model<sup>32,31,33</sup>:  $\boldsymbol{\sigma}_p = 2\nu_{p,k} \mathbf{S}_p$ , where  $\nu_{p,k}$  is the kinetic part of particle-phase kinematic viscosity<sup>32</sup>, and the particle-phase strain-rate tensor is defined by  $\mathbf{S}_p = \frac{1}{2} [\nabla \mathbf{U}_p + (\nabla \mathbf{U}_p)^T - \frac{2}{3} (\nabla \cdot \mathbf{U}_p) \mathbf{I}]$ . Thus, the decomposition can be rewritten as a pressure term and a viscous term, i.e.  $\mathbf{P}_p = p_{p,k} \mathbf{I} - 2\nu_{p,k} \mathbf{S}_p$ , where the kinetic contribution to the granular pressure  $p_{p,k} = \Theta_p$ . Similar to  $\mathbf{P}_p$ , the collisional flux tensor is also decomposed into two components:  $\mathbf{G}_p = p_{p,c} \mathbf{I} - 2\nu_{p,c} \mathbf{S}_p$ , where  $p_{p,c}$  is the collisional contribution to the granular pressure and  $\nu_{p,c}$  is collisional shear kinematic viscosity<sup>32</sup>. In the strongly collisional regime,  $\mathbf{P}_p$  is nearly isotropic, so the transport equation for  $\Theta_p$  is solved instead of  $\mathbf{P}_p$  in TFM, which is the trace of Eq. (25):

$$\begin{aligned} \frac{\partial \rho_p \alpha_p \Theta_p}{\partial t} + \nabla \cdot \rho_p \alpha_p \left( \mathbf{U}_p \Theta_p - \frac{2}{3} k_p \nabla \Theta_p \right) + \frac{2}{3} \rho_p \alpha_p [(p_{p,k} + p_{p,c}) \mathbf{I} - 2(\nu_{p,k} + \nu_{p,c}) \mathbf{S}_p] : \nabla \mathbf{U}_p \\ = -\rho_p \alpha_p \frac{2}{\tau_p} \Theta_p - \rho_p \alpha_p \frac{(1 - e^2)}{\tau_c} \Theta_p. \end{aligned} \quad (27)$$

The particle-phase conductivity also has kinetic and collisional contributions<sup>32</sup>:  $k_p = k_{p,k} + k_{p,c}$ . Under this framework, different models can be used to calculate the kinetic theory coefficients mentioned above. An example set of these coefficients is given in Table 1<sup>32</sup>, in which  $\nu_{p,b}$  is the bulk kinematic viscosity.

Both AG and TFM simulations presented in this work are performed using codes implemented in OpenFOAM, an open-source CFD package<sup>44</sup>. Note that first-order spatial reconstruction schemes are used for the convective fluxes when solving the EE models.

## Simulation Cases

### One-way Coupled Homogeneous Isotropic Turbulence

For this case, a two-dimensional frozen turbulence field is generated by constructing a random, periodic vorticity field on a domain ( $L_x = L_y = 2\pi$ ,  $n_x = n_y = 512$ ) with Fourier coefficients  $|\hat{\omega}| \in [0, 5]$ . The vorticity field is then projected onto a divergence-free velocity field for wavevectors  $|\kappa| < 16$ . The velocity field is advanced to  $t = 0.0718$  using single-phase, incompressible Navier–Stokes, with viscosity  $\nu = 0.1387$ . The velocity field is then duplicated in the  $z$ -direction to  $L_z = \frac{3}{16}\pi$ ,  $n_z = 48$ . Particles are then randomly distributed within the domain while the fluid-phase velocity field is held constant.

This method gives a velocity field with Taylor microscale Reynolds number  $Re_\lambda = 18.96$ , Taylor microscale  $\lambda_f = 0.4486$ , and Kolmogorov time scale  $\tau_\eta = 0.02817$ . We obtain coarser velocity fields using box filtering and finer fields using linear interpolation. The coarsest field is resolved up to  $\kappa_{\max}\eta = 2$ , where  $\kappa_{\max} = n_x \cdot \pi \cdot L_x$  is the maximum wavenumber. Table 2 summarizes the HIT simulation cases.

Due to the fast convergence of EL, we only perform EL simulations up to  $n_x = 512$ . For the EE methods, we also perform  $n_x = 1024$  and  $n_x = 2048$  simulations. After seeding the domain with particles, we advance the simulation to time  $t = 1.0718$ . We gather statistics and perform our analysis at this time. Because these simulations are homogeneous, we approximate the ensemble average as a spatial average over the domain:  $\langle \phi \rangle = \int \phi d\mathbf{x}$ .

### Two-way Coupled Cluster-induced Turbulence

Two-way coupled simulations of CIT are performed under grid refinement for EL and EE. We start with a periodic domain of fluid, seeded homogeneously with particles. The particles fall under gravity while the fluid is kept statistically stationary by an additional source term in the fluid-phase momentum equation. Once the flow reaches a statistically stationary state, we compute the various statistics. For EL, we also compare several fixed and variable width

Gaussian filters in computing those statistics. We employ similar parameters as Capecelatro et al.<sup>45</sup>, as summarized in Table 3. Because CIT is homogeneous and reaches a statistically stationary state, we approximate the ensemble average for these simulations as a spatial and temporal average:  $\langle \phi \rangle = \int_{T_i}^{T_f} \int \phi d\mathbf{x} dt$  over the domain and over a long  $T_f - T_i$ .

Due to fluid–particle coupling, the choice of volume filtering kernel in the EL simulations  $\mathcal{H}$  during run time can affect EL simulations, especially for the two-way coupled CIT simulations. However, we find EL simulations to be fairly insensitive to  $\mathcal{H}$ . We performed  $d_p/\Delta = 1/4$  resolution simulations of CIT using Gaussian kernels for  $\mathcal{H}$  with varying widths,  $\delta_f$ . To isolate the effect of  $\mathcal{H}$ , we can consider statistics from the ensemble of particles because they are not computed via density estimation. The average particle velocity and variance of the particle velocity components are shown in Table 4. These do not show strong dependence on  $\delta_f$ , so we assume our CIT simulations have “converged” under changes in the volume filtering kernel to the correct solution. We focus hereinafter on the effect of filter size on obtaining Eulerian statistics from the simulation data.

## Results and Discussion

### Instantaneous Particle Fields

For particles in frozen HIT, Figs. 2, 3, and 4 show snapshots of the particle field for the three methods under refinement.  $\alpha_p$  is shown for the EE methods and the particle locations for EL. The results demonstrate the expected preferential concentration phenomenon for all three methods. The moderate  $St = 1$  particles cluster strongly compared to the  $St = 0.2$  and  $St = 5$  particles. For the  $St = 0.2$  particles, the low-resolution AG simulations develop sharp regions of accumulation inside dilute regions. For the higher resolution simulations of the same  $St$  cases, few differences are found between AG and TFM. The  $St = 5$  simulations demonstrate the significant differences between AG and TFM simulations. The TFM simulations appear smoother, eventually reaching convergence, while the AG simulations show sharp gradients

that remain under-resolved, even at  $d_p/\Delta = 4$ . For all three methods, the higher resolution simulations support finer structures. This is especially prominent in the  $St = 0.2$  case, but less clear in the  $St = 5$  particles. EL simulations at grid resolutions  $d_p/\Delta = 1/2$  and  $d_p/\Delta = 1$  show no significant differences for any  $St$  particles, suggesting convergence for this method.

The CIT particle fields are shown in Fig. 5. The higher resolution EE simulations appear to show finer structures compared to the lower resolution simulations. For  $d_p/\Delta = 1/8$ , the volume fraction field in TFM fails to develop fluctuations and in AG develops into a single, horizontal, domain-constrained wave. Qualitatively, EL simulations appear similar at all resolutions examined.

### Filter Sensitivity in EL

Depending on the simulation, results from EL can vary strongly with the choice of post-processing filter. Fig. 6 shows the variance in volume fraction and the granular temperature from EL simulations of the  $St = 0.2$ ,  $St = 1$ , and  $St = 5$  particles. Note for the Fix 1 filter (see the Fig. 6 caption for details on the nomenclature), the filter width is under-resolved for all except the highest resolution simulation.

The volume-fraction variance for the moderate Stokes number case covers almost a decade, for the filters tested. Even for the low- and high-Stokes cases, there is a factor of about 3 between the variance captured by the narrowest and the widest filters. Capturing the granular temperature is even more problematic.  $3 \langle \Theta_p \rangle_p / 2\kappa$  ranges between 0 and up to 30% depending on the filter used and the Stokes number of the particles. Because lower Stokes number particles follow fluid streamlines more closely, the granular temperature should be small. But for kernel density estimation, the wider filters suggest that granular temperature decreases with Stokes number. For example, using Var 100,  $3 \langle \Theta_p \rangle_p / 2\kappa_p$  decreases from around 0.3 to 0.15 going from the low to the high Stokes number case. If a wider filter is used, it will sample from particles that are far separated. Low-Stokes-number particles follow the fluid closely, so these wider filters are including in the granular temperature a large contribution from the fluid velocity variation.



Narrower filters recover the expected behavior that higher Stokes number particles generate more granular temperature. However, extremely narrow filters give zero granular temperature, regardless of the Stokes number.

In the limit of a zero-width filter, the estimated density can be expected to become identical to Eq. (11) and the volume fraction will approach a sum of Dirac functions. Since these functions are not square integrable, the volume-fraction variance will diverge. In the same limit, granular temperature will approach zero. In the limit of an infinite filter width, the volume-fraction variance will approach zero and  $3 \langle \Theta_p \rangle_p$  will approach  $2\kappa_p$ . This can be shown from Eqs. (13)–(15).

For HIT, statistics computed with the variable-width filters appear to still have significant parameter sensitivity. Although the Voronoi technique is parameter-free, it effectively behaves as a narrow filter. It predicts high volume-fraction variance and low granular temperature, similar to the narrowest Gaussian filters. There does not appear to be a unique way to choose the number density estimation technique, but the fixed and variable width kernel density estimation approaches provide flexibility by exposing the controlling parameter, either  $h$  for the fixed-width method or  $\mathcal{N}_p$  for the variable-width method.

In contrast to HIT, one-point CIT statistics gathered from EL, shown in Fig. 7, indicate less sensitivity to the filter. Volume-fraction variance is converged for all except the narrowest fixed filter. Granular temperature is still filter dependent in CIT, but not as much as in HIT. The poor performance of NDF estimation in HIT may be attributed to the appearance of, comparatively, highly anisotropic clusters, as evident in the particle fields shown in Figs. 2, 3, 4, and 5.

The energy spectra of the volume fraction can identify the advantages of the variable width filter. The energy spectrum of volume fraction and the particle velocity are computed as

$$E_\alpha = \langle |\text{FFT} \{ \alpha'_p \} |^2 \rangle, \quad (28)$$

$$\text{and } E_{U_{p,i}} = \frac{1}{\langle \alpha_p \rangle} \langle |\text{FFT} \{ \sqrt{\alpha_p} (U_{p,i} - \langle U_{p,i} \rangle_p) \} |^2 \rangle. \quad (29)$$

HIT is isotropic in the  $x$ - $y$  plane, so we perform the fast Fourier transform (FFT) over these directions and average over the wavevector orientations and in the  $z$  direction. For CIT, we perform the FFT in the vertical direction and average over the other two directions and over time.

For the highest resolution HIT simulations, spectra of the particle volume fraction are shown in Fig. 8. While the variable-width filters show significant parameter sensitivity, the fixed-width filters are significantly more dependent on the filter width. Compared to results from HIT, the CIT volume fraction and vertical velocity spectra in Fig. 9 show better agreement between filters, especially at large scales (low wavenumbers).

Because of the filter sensitivity, comparisons between EL and the EE methods require care. Averages over particle ensembles can be compared directly to particle-phase-averaged quantities from EE. The particle-phase-averaged particle velocity and the average particle velocity over the ensemble of particles are equal:  $\langle \mathbf{v} \rangle = \langle \mathbf{U}_p \rangle_p$ . Similarly, the total particle fluctuating energy can be computed equivalently in the Eulerian and Lagrangian frames. This can be seen from Eq. (22). Figure 10 shows comparisons of these statistics between the three methods in the CIT and HIT simulations. For all three  $St$  particles, the EL and EE methods report similar total particle fluctuating energies, particularly in the highly resolved simulations. CIT simulations exhibit close agreement between the AG and EL simulations. For highly resolved simulations, the TFM simulation under-predicts the particle settling speed compared to EL and AG. As suggested by Kong et al.<sup>23</sup>, AG allows for more anisotropic clusters that align in the vertical direction and fall faster than the more globular clusters found in TFM simulations. AG also predicts closer total particle fluctuating energy to EL. These results suggests AG has advantages over TFM in flows with strong anisotropy, such as CIT.

### Statistical Convergence under Grid Refinement

For particles in frozen HIT, the computed statistics establish convergence for EL. Figure 6 shows that for a given filter, EL one-point statistics converge under grid refinement. Figure 11

shows that, for EL simulations of HIT, the volume-fraction power spectra match for all scales, regardless of the grid resolution.

In contrast to EL, convergence of EE simulations is problem dependent. In HIT, the volume-fraction variance increases linearly with grid resolution for both AG and TFM, as shown in Fig. 12, except for the  $St = 5$  TFM simulation. For granular temperature, TFM and AG demonstrate contradictory trends under refinement. This is due to the fact that the mechanism of generation of granular energy in TFM and AG is fundamentally different. In TFM, the primary mechanism stems from the divergence of particle velocity. TFM shows almost zero granular temperature for the low-Stokes-number particles because the particles follow fluid streamlines well, so the particle velocity divergence is zero. At higher Stokes numbers, the particles can deviate from the fluid streamlines, so granular temperature is produced in regions of particle velocity divergence. The granular temperature is low in coarse simulations because the particle velocity field is smoother than in fine-mesh simulations, as can be expected due to numerical dissipation. In contrast to TFM, AG includes the full particle pressure tensor, so AG can model some of the physics of a multi-valued velocity field<sup>23</sup>. AG can generate granular temperature from regions of PTC and these regions are not necessarily regions of large velocity divergence. On coarse meshes, the particles are more susceptible to PTC because the fluid velocity is sampled with fewer grid cells. Some fluid variation is lost on these coarser grids, so the fluid will be able to build more particle momentum. The particles will have more momentum to deviate from the fluid streamlines, and cross trajectories. Since the PTC is more common on coarser meshes, the granular temperature is found to decrease with grid resolution for AG.

HIT volume-fraction spectra, shown in Fig. 11, also demonstrate lack of convergence. The  $St = 0.2$  AG simulations appear to have more energy in the high-wavenumber fluctuations for lower-resolution simulations. As discussed earlier, these simulations tend to form sharp regions of accumulation inside dilute regions that disappear under refinement. It is possible that these lower-Stokes-number simulations using AG are prone to this behavior because low-Stokes-number flows have lower granular temperature. In dilute regions, AG may suffer from

weak hyperbolicity, if the granular temperature is low, and degenerate to the monokinetic, pressure-less gas equations. Finer simulations reduce the regions of PTC, so the associated degeneracy is avoided and the accumulation regions disappear. In contrast, high-Stokes-number particles may generate enough granular temperature to retain strong hyperbolicity in AG, so these simulations do not develop these clumps of particles.

The  $St = 5$  AG volume-fraction spectra appear to generate more energy in the higher wavenumbers as the resolution increases. As discussed previously, sharp gradients in the volume fraction field are evident in these simulations. In contrast, the spectra from the  $St = 5$  TFM simulation indicate convergence. However, this convergence may not be to a physically correct solution. Discontinuous solutions to the Boltzmann equation are possible, even with smooth initial conditions. If this is the case for the  $St = 5$  particles, EE methods should not converge under refinement. AG may give the correct behavior under refinement while TFM gives non-physically smooth solutions.

CIT simulations pose fewer convergence difficulties than HIT, which is due to the fact that kinetic energy in the system is mainly dissipated through gas viscous effects in CIT, instead of particle collisions in HIT. Figure 13 shows one-point statistics from these simulations. The volume-fraction variance appears converged for EL and TFM, and appears to be approaching convergence for AG. Due to the density estimation dependence, it is again difficult to compare EL to AG and TFM for granular temperature. However, the volume fraction variance is similar for AG and EL, indicating similar degrees of clustering. AG also gives a prediction for anisotropy in the particle pressure tensor. TFM is not capable of making a similar prediction.

The CIT volume fraction and vertical velocity spectra are shown in Figure 14. For all except the coarsest mesh, the EL spectra converge. At low wavenumbers, AG and TFM both appear converged, and predict similar power. Again, because of the filter dependence at high wavenumbers, it is difficult to compare EL to AG and TFM.

Taken together, these results show that, at least for particles in frozen HIT, EE simulations face similar difficulties as faced by traditional EL simulations. Grid-refinement behavior in

traditional EL can be replicated by computing statistics under shrinking fixed filters. A statistic computed from an EE simulation with resolution  $d_p/\Delta$  can be compared to the statistic from the EL simulation using fixed-width density estimation with the analogous  $d_p/h$ .  $\Delta$  and  $h$  are not exactly equivalent here, but this allows us to qualitatively compare traditional EL to EE. The volume-fraction variance and granular temperature comparison between the three methods, Fig. 12, shows that statistics from AG behave much like statistics from EL under shrinking filters. If we use  $\Lambda$  to denote  $\Delta$  for EE and  $h$  for EL, we see that for both EE and EL, the volume-fraction variance increases with  $d_p/\Lambda$ , and the granular temperature decreases with  $d_p/\Lambda$ . Since  $d_p/\Lambda$  can either represent a resolution or a filter width, we can observe a filter-like behavior in the EE methods. An EE “filter” width, related to the grid resolution, would be tied to the numerical scheme used in the EE solvers.

## Conclusions

This paper studies verification of three methods of simulating fluid–particle flows, TFM, AG, and EL. Both TFM and EL are commonly used for these simulations and AG has recently shown promising results in this field. Here, we study two aspects of verification. First, we find that, depending on the type of simulation, recovering statistics from EL simulations cannot be performed uniquely. Although EL can produce physically faithful simulation results, and may serve as a benchmark for EE, difficulty extracting statistics from EL poses a challenge for informing fluid–particle models. While CIT is less dependent on the density estimation technique, HIT is heavily dependent. Second, we find that volume-filtered EL is capable of grid convergence in both HIT and CIT. Convergence for the EE methods is poor for HIT, but better for CIT. CIT results from EL and AG agree better with each other than with results from TFM.

Future work for EL may focus on alternative methods for density estimation. The statistics literature has introduced many techniques, possibly useful for extracting statistics from problematic EL simulations like HIT. However, the relative ease of CIT simulations suggests that careful selection of simulation conditions, statistics to analyze, and post-processing parameters,

can circumvent convergence difficulties with AG and parameter sensitivity with EL. EL and AG simulations of problems like CIT may still provide useful results for fluid–particle macroscale models.

## Acknowledgments

The authors gratefully acknowledge the financial support from the U.S. National Science Foundation under Grants CBET-1437865 and CBET-1437903. This research was also partially supported (B.K. and R.O.F.) by the U.S. Department of Energy, National Energy Technology Laboratory (NETL) through the Ames Laboratory. The Ames Laboratory is operated for the U.S. Department of Energy by Iowa State University under Contract DE-AC02-07CH11358.

## Literature Cited

- 1 Jackson R. *The Dynamics of Fluidized Particles*. Cambridge Monographs on Mechanics. Cambridge, UK: Cambridge University Press. 2000.
- 2 Tenneti S, Subramaniam S. Particle-resolved direct numerical simulation for gas–solid flow model development. *Annual Review of Fluid Mechanics*. 2014;46:199–230.
- 3 Uhlmann M, Doychev T. Sedimentation of a dilute suspension of rigid spheres at intermediate Galileo numbers: the effect of clustering upon the particle motion. *J Fluid Mech*. 2017; 752:310–348.
- 4 Fox RO. On multiphase turbulence models for collisional fluid–particle flows. *Journal of Fluid Mechanics*. 2014;742:368–424.
- 5 Igci Y, Andrews AT, Sundaresan S, Pannala S, O'Brien T. Filtered two-fluid models for fluidized gas-particle suspensions. *AIChE Journal*. 2008;54(6):1431–1448.
- 6 Lu L, Konan A, Benyahia S. Influence of grid resolution, parcel size and drag models on bubbling fluidized bed simulation. *Chemical Engineering Journal*. 2017;.

- 7 Agrawal K, Loezos PN, Syamlal M, Sundaresan S. The role of meso-scale structures in rapid gas–solid flows. *Journal of Fluid Mechanics*. 2001;445:151–185.
- 8 Balachandar S, Eaton JK. Turbulent dispersed multiphase flow. *Annual Review of Fluid Mechanics*. 2010;42:111–133.
- 9 Capecelatro J, Desjardins O, Fox RO. Numerical study of collisional particle dynamics in cluster-induced turbulence. *Journal of Fluid Mechanics*. 2014;747(R2).
- 0 Subramaniam S. Lagrangian–Eulerian methods for multiphase flows. *Progress in Energy and Combustion Science*. 2013;39(2):215–245.
- 1 Balachandar S. A scaling analysis for point–particle approaches to turbulent multiphase flows. *International Journal of Multiphase Flow*. 2009;35(9):801–810.
- 2 Garg R, Narayanan C, Lakehal D, Subramaniam S. Accurate numerical estimation of inter-phase momentum transfer in Lagrangian–Eulerian simulations of dispersed two-phase flows. *International Journal of Multiphase Flow*. 2007;33(12):1337–1364.
- 3 Garg R, Narayanan C, Subramaniam S. A numerically convergent Lagrangian–Eulerian simulation method for dispersed two-phase flows. *International Journal of Multiphase Flow*. 2009;35(4):376–388.
- 4 Capecelatro J, Desjardins O. An Euler-Lagrange strategy for simulating particle-laden flows. *Journal of Computational Physics*. 2013;238:1–31.
- 5 Ireland PJ, Desjardins O. Improving particle drag predictions in Euler–Lagrange simulations with two-way coupling. *Journal of Computational Physics*. 2017;338:405–430.
- 6 Kong B, Fox RO. A solution algorithm for fluid–particle flows across all flow regimes. *Journal of Computational Physics*. 2017;(in revision).

- 7 Passalacqua A, Fox RO. Simulation of mono- and bidisperse gas-particle flow in a riser with a third-order quadrature-based moment method. *Industrial & Engineering Chemistry Research*. 2012;52(1):187–198.
- 8 Passalacqua A, Galvin JE, Vedula P, Hrenya CM, Fox RO. A quadrature-based kinetic model for dilute non-isothermal granular flows. *Communications in Computational Physics*. 2011;10(01):216–252.
- 9 Yuan C, Fox RO. Conditional quadrature method of moments for kinetic equations. *Journal of Computational Physics*. 2011;230(22):8216–8246.
- 0 Vié A, Chalons C, Fox RO, Laurent F, Massot M. A multi-Gaussian quadrature method of moments for simulating high Stokes number turbulent two-phase flows. In: *Annual Research Brief*. Center for Turbulence Research, Stanford University. 2012;.
- 1 Chalons C, Fox RO, Massot M. A multi-Gaussian quadrature method of moments for gas-particle flows in a LES framework. In: *Proceedings of the Summer Program*. Center for Turbulence Research, Stanford University. 2010; pp. 347–358.
- 2 Vié A, Doisneau F, Massot M. On the anisotropic Gaussian velocity closure for inertial-particle laden flows. *Communications in Computational Physics*. 2015;17(01):1–46.
- 3 Kong B, Fox RO, Feng H, Capecelatro J, Patel R, Desjardins O. Euler-Euler anisotropic Gaussian mesoscale simulation of homogeneous cluster-induced gas-particle turbulence. *AIChE Journal*. 2017;63(7):2630–2643.
- 4 Gualtieri P, Picano F, Sardina G, Casciola CM. Exact regularized point particle method for multiphase flows in the two-way coupling regime. *J Fluid Mech*. 2015;773:520–561.
- 5 Subramaniam S. Statistical modeling of sprays using the droplet distribution function. *Physics of Fluids*. 2001;13(3):624–642.



- 6 Fox RO. Turbulence in multiphase flows: Fundamental modeling aspects. In: *Handbook of Multiphase Flow Science and Technology*, edited by Yeoh GH, pp. 1–63. Singapore: Springer Nature. 2017;.
- 7 Rani SL, Balachandar S. Preferential concentration of particles in isotropic turbulence: A comparison of the Lagrangian and the equilibrium Eulerian approaches. *Powder Technology*. 2004;141(1-2):109–118.
- 8 Maxey MR. The gravitational settling of aerosol particles in homogeneous turbulence and random flow fields. *Journal of Fluid Mechanics*. 1987;174(-1):441.
- 9 Toschi F, Bodenschatz E. Lagrangian properties of particles in turbulence. *Annual Review of Fluid Mechanics*. 2009;41(1):375–404.
- 0 Syamlal M, Rogers W, O'Brien TJ. MFIx documentation: Theory guide. *National Energy Technology Laboratory, US Department of Energy, Technical Note DOE/METC-95/1013 and NTIS/DE95000031*. 1993;.
- 1 Gidaspow D. *Multiphase Flow and Fluidization: Continuum and Kinetic Theory Descriptions*. New York, USA: Academic Press. 1994.
- 2 Garzó V, Tenneti S, Subramaniam S, Hrenya CM. Enskog kinetic theory for monodisperse gas–solid flows. *Journal of Fluid Mechanics*. 2012;712:129–168.
- 3 Jenkins JT, Savage SB. A theory for the rapid flow of identical, smooth, nearly elastic, spherical particles. *Journal of Fluid Mechanics*. 1983;130:187–202.
- 4 Anderson TB, Jackson R. Fluid mechanical description of fluidized beds. Equations of motion. *Industrial & Engineering Chemistry Fundamentals*. 1967;6(4):527–539.
- 5 Gibilaro LG, Gallucci K, Di Felice R, Pagliai P. On the apparent viscosity of a fluidized bed. *Chemical Engineering Science*. 2007;62(1):294–300.

- 6 Monchaux R, Bourgoïn M, Cartellier A. Preferential concentration of heavy particles: A Voronoï analysis. *Physics of Fluids*. 2010;22.
- 7 Tagawa Y, Mercado JM, Prakash VN, Calzavarini E, Sun C, Lohse D. Three-dimensional Lagrangian Voronoï analysis for clustering of particles and bubbles in turbulence. *Journal of Fluid Mechanics*. 2012;693:201–215.
- 8 Capecelatro J, Desjardins O, Fox RO. On fluid–particle dynamics in fully developed cluster-induced turbulence. *Journal of Fluid Mechanics*. 2015;780:578–635.
- 9 Desjardins O, Blanquart G, Balarac G, Pitsch H. High order conservative finite difference scheme for variable density low Mach number turbulent flows. *Journal of Computational Physics*. 2008;227(15):7125–7159.
- 0 Rycroft C. Voro++: a three-dimensional Voronoi cell library in C++. *Lawrence Berkeley National Laboratory*. 2009;.
- 1 Bhatnagar PL, Gross EP, Krook M. A model for collision processes in gases. I. Small amplitude processes in charged and neutral one-component systems. *Physical Review*. 1954; 94(3):511.
- 2 Marchisio DL, Fox RO. *Computational Models for Polydisperse Particulate and Multiphase Systems*. Cambridge, UK: Cambridge University Press. 2013.
- 3 Carnahan NF, Starling KE. Equation of state for nonattracting rigid spheres. *The Journal of Chemical Physics*. 1969;51(2):635–636.
- 4 Weller HG, Tabor G, Jasak H, Fureby C. A tensorial approach to computational continuum mechanics using object-oriented techniques. *Computers in Physics*. 1998;12(6):620–631.
- 5 Capecelatro J, Desjardins O, Fox RO. Effect of domain size on fluid–particle statistics in homogeneous, gravity-driven, cluster-induced turbulence. *Journal of Fluids Engineering*. 2015;138(4):041301.

## List of Figures

1	Comparison of density estimation techniques. Left: histogram. Center: Gaussian filter. Right: Voronoi tessellation. . . . .	29
2	$St = 0.2$ particle fields at $t = 1$ for TFM, AG, EL (left to right) and increasing resolution (top to bottom) for HIT case. $\alpha_p$ shown for EE methods and particle locations for EL method. . . . .	30
3	$St = 1$ particle fields at $t = 1$ for TFM, AG, EL (left to right) and increasing resolution (top to bottom) for HIT case. $\alpha_p$ shown for EE methods and particle locations for EL method. . . . .	31
4	$St = 5$ particle fields at $t = 1$ for TFM, AG, EL (left to right) and increasing resolution (top to bottom) for HIT case. $\alpha_p$ shown for EE methods and particle locations for EL method. . . . .	32
5	CIT particle fields for TFM, AG, EL (top to bottom) and increasing resolution (left to right). . . . .	33
6	Volume-fraction variance (left) and granular temperature (right) from HIT simulations for three $St$ particles (top to bottom). Statistics are captured using the various density estimation techniques shown in the legend. Fix and Var refer to kernel density estimation using fixed filter width and variable filter width, respectively. In the case of Fix, the number following refers to the filter width, in multiples of particle diameter, $h/d_p$ , and in the case of Var, the number refers to the number of particles sampled, $\mathcal{N}_p$ . . . . .	34
7	Volume-fraction variance (left) and granular temperature (right) from CIT simulations. The NDF estimation techniques used are the same as those used for the HIT simulations, excluding the Voronoi technique. The legend is shown previously, in Figure 6. . . . .	35
8	$\alpha_p$ spectra for EL simulations of HIT at resolution $d_p/\Delta = 2$ using fixed (left) and variable (right) width filters for the three $St$ particles (top to bottom). . . . .	36
9	$\alpha_p$ (top) and $U_{p,x}$ (bottom) spectra for EL simulations of CIT at resolution $d_p/\Delta = 1$ using fixed (left) and variable (right) filters. . . . .	37
10	HIT (left) and CIT (right) one-point statistics from the three methods. The total particle fluctuating energy, $\kappa_p$ is shown for HIT. The particle settling speed, $\langle U_{p,x} \rangle_p$ , and total particle fluctuating energy are shown for CIT. These statistics do not depend on the EL filter. . . . .	38
11	$\alpha_p$ spectrum from the three methods (left to right) and the three particle Stokes numbers (top to bottom) for HIT case. Spectra are shown for increasing grid resolution. For EL, Fix 10 was used for density estimation. Darker lines refer to higher resolutions. For TFM and AG, the black dashed lines are from the highest resolution EL simulation for comparison. . . . .	39
12	HIT one-point statistics vs. grid resolution for EE methods and filter width for EL method using fixed width filters. Particle volume-fraction variance (left) and granular temperature (right). $\Lambda$ refers to grid resolution, $\Delta$ , for EE methods and filter width, $h$ , for EL. . . . .	40

- 13 CIT one-point statistics. Volume-fraction variance (top left), granular temperature (top right), and anisotropy in particle pressure tensor (bottom). For EL, Fix 10 was used for density estimation. . . . . 41
- 14  $\alpha_p$  (top) and  $U_{p,x}$  (bottom) spectra from the three methods (left to right) for CIT case. Spectra are shown for increasing grid resolution. For EL, Fix 10 was used for density estimation. Per row, the black lines are from the highest resolution EL simulation for comparison. . . . . 42

Accepted Article

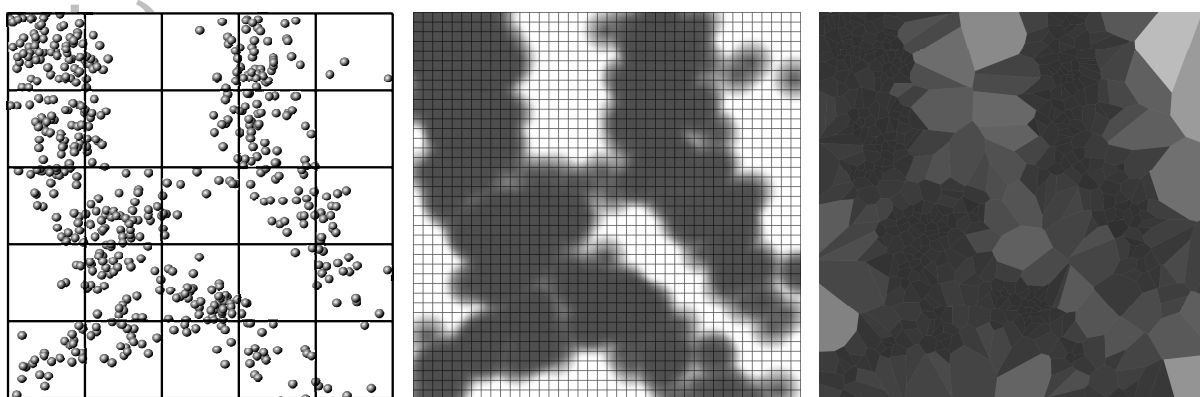


Figure 1: Comparison of density estimation techniques. Left: histogram. Center: Gaussian filter. Right: Voronoi tessellation.

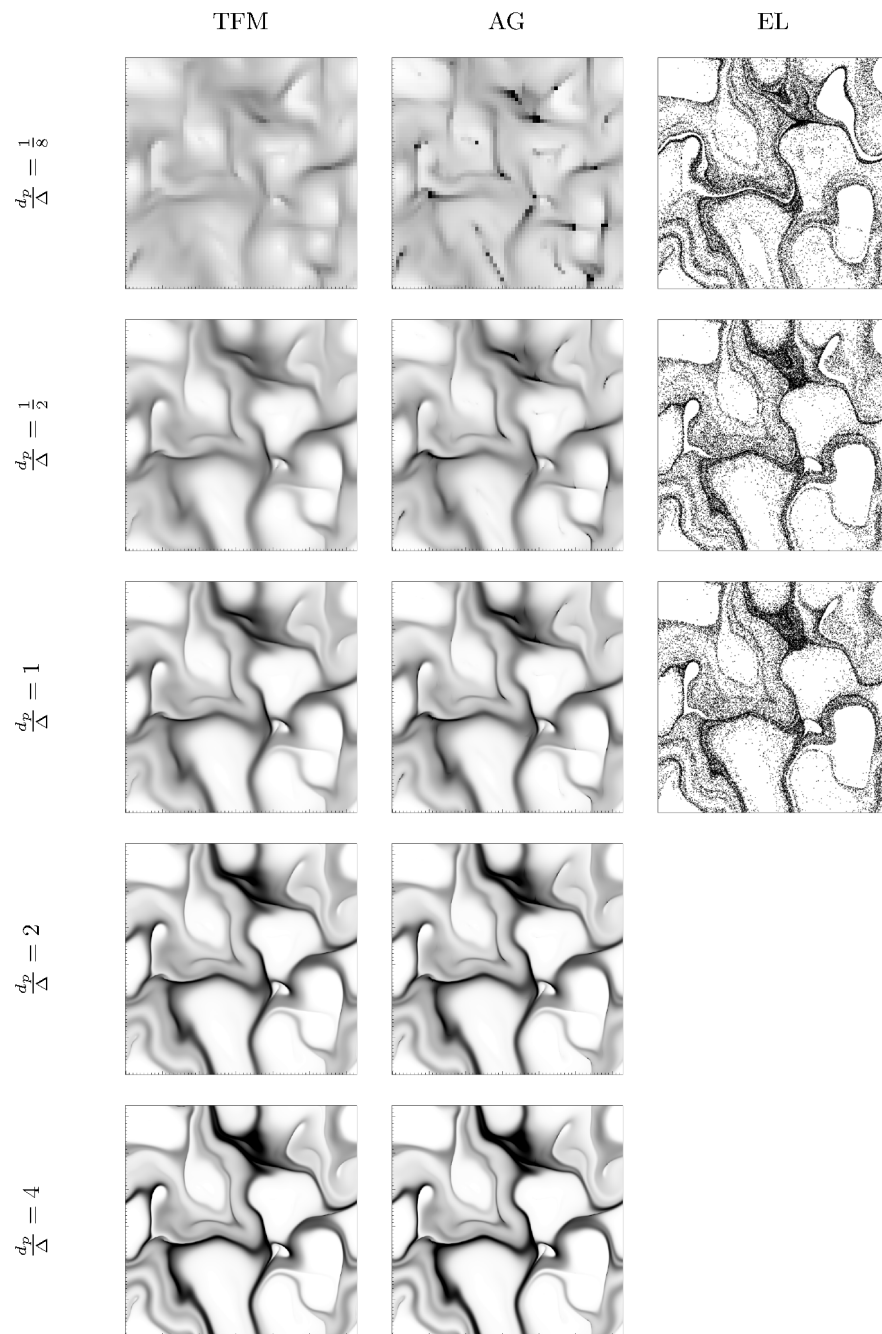


Figure 2:  $St = 0.2$  particle fields at  $t = 1$  for TFM, AG, EL (left to right) and increasing resolution (top to bottom) for HIT case.  $\alpha_p$  shown for EE methods and particle locations for EL method.

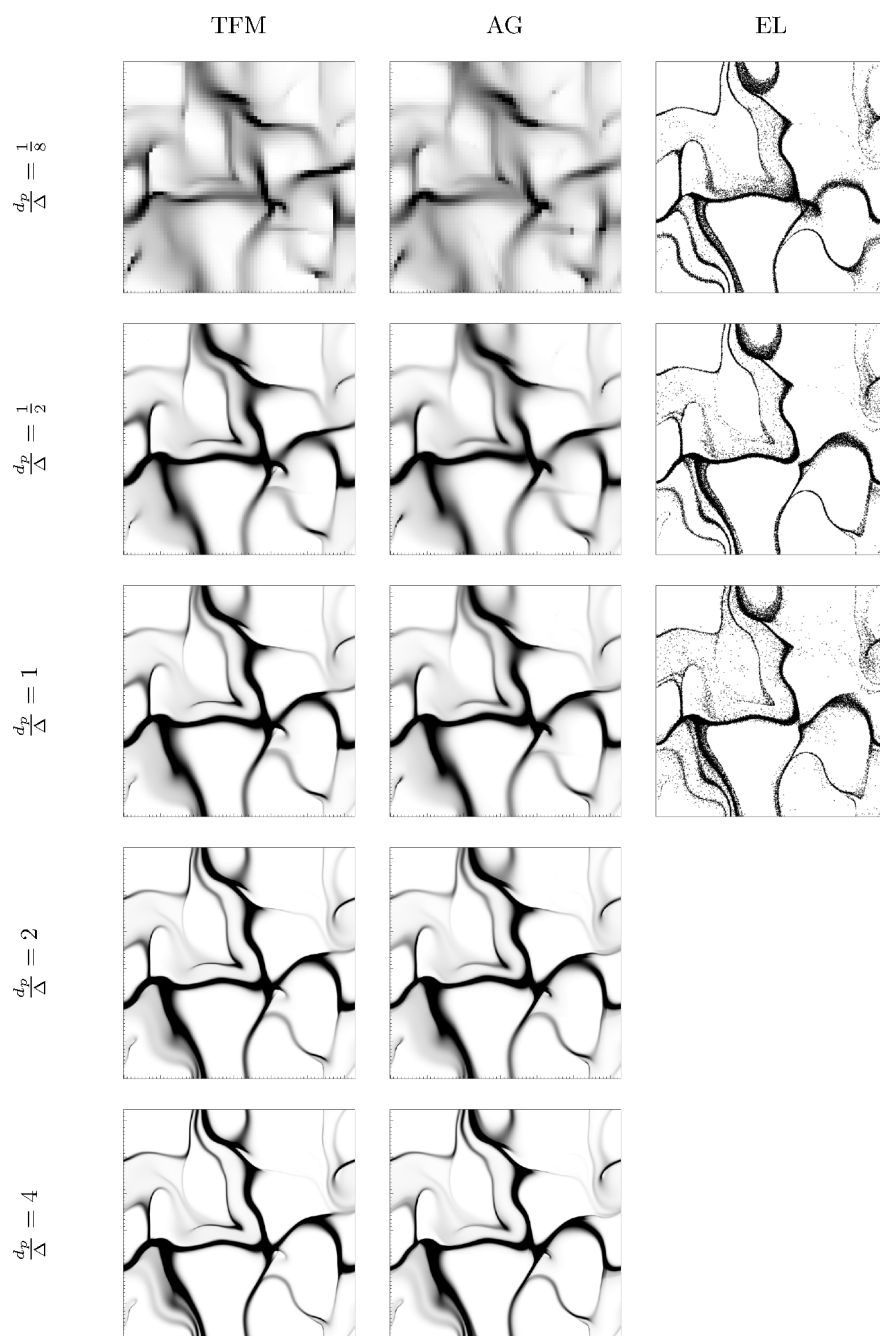


Figure 3:  $St = 1$  particle fields at  $t = 1$  for TFM, AG, EL (left to right) and increasing resolution (top to bottom) for HIT case.  $\alpha_p$  shown for EE methods and particle locations for EL method.

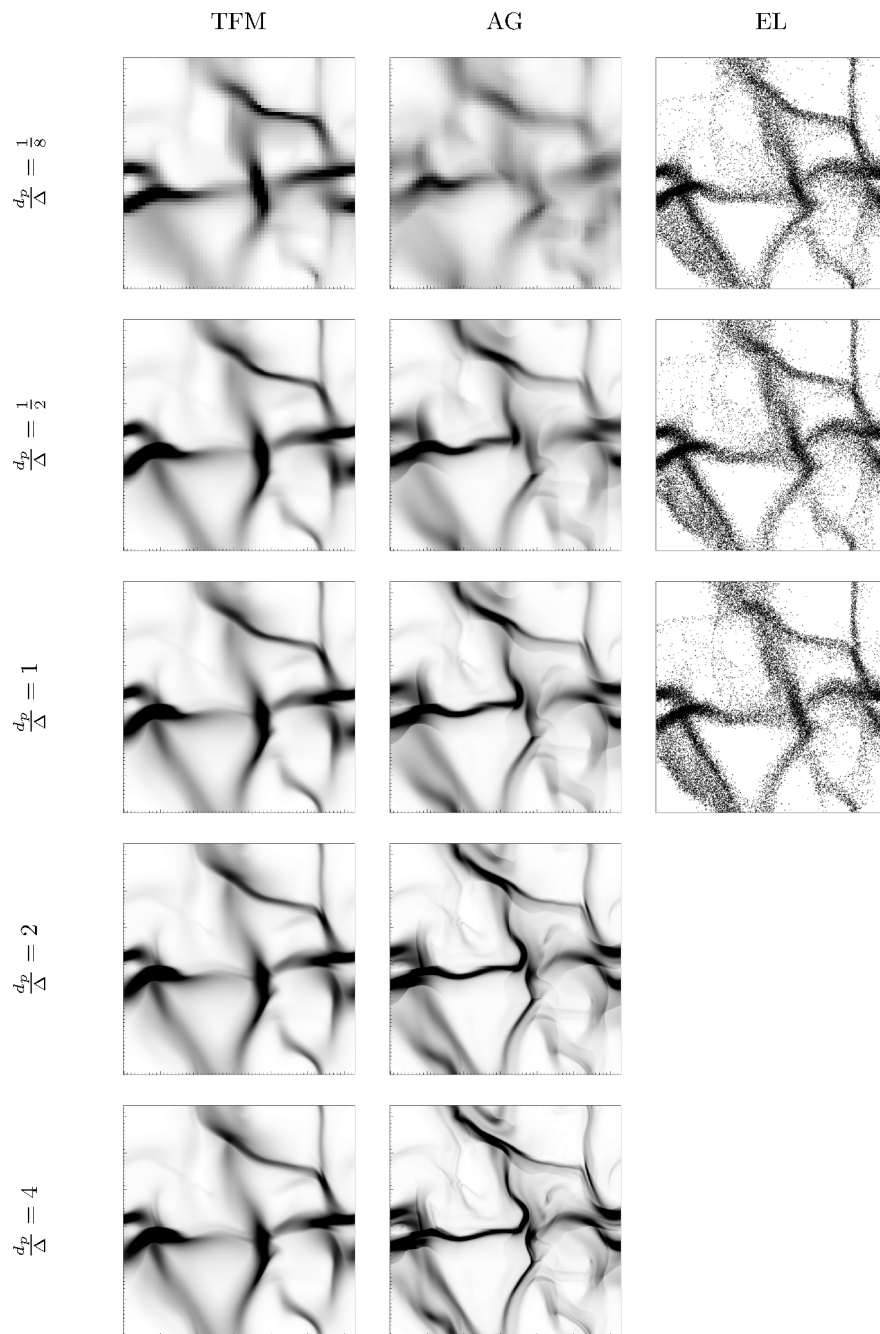


Figure 4:  $St = 5$  particle fields at  $t = 1$  for TFM, AG, EL (left to right) and increasing resolution (top to bottom) for HIT case.  $\alpha_p$  shown for EE methods and particle locations for EL method.



Accepted Article

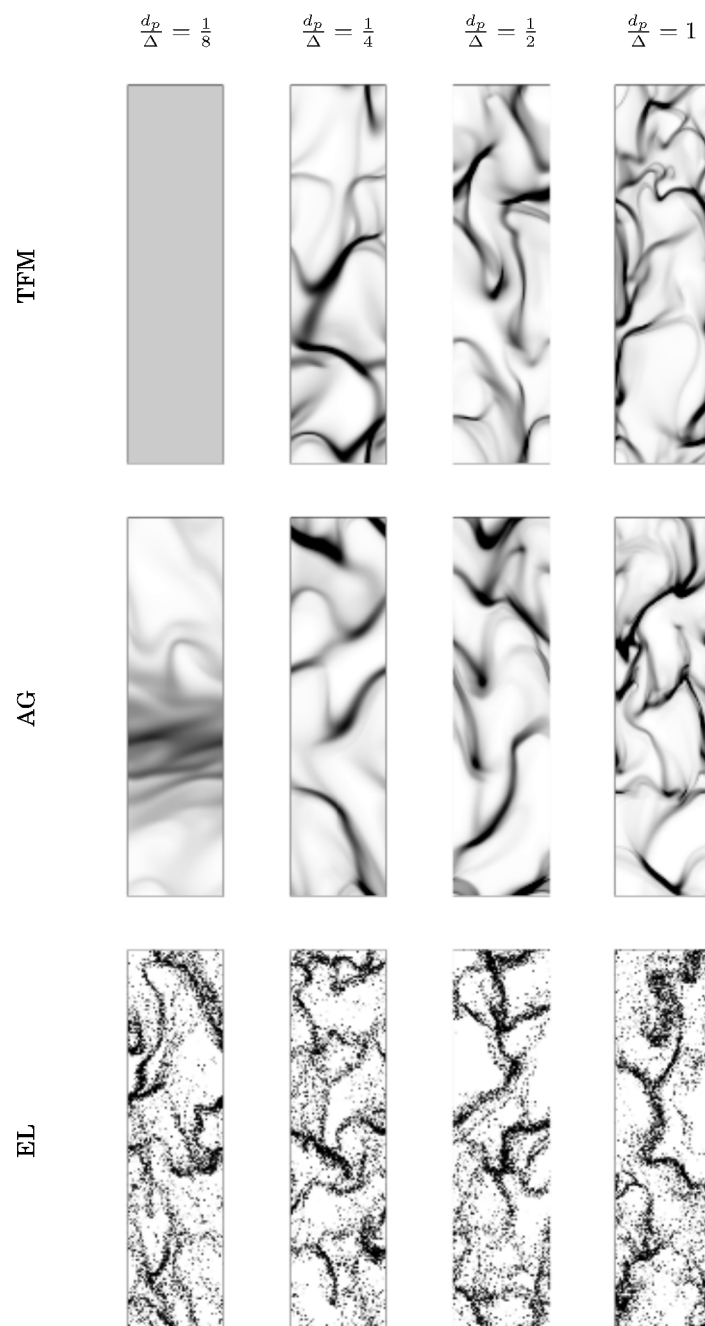


Figure 5: CIT particle fields for TFM, AG, EL (top to bottom) and increasing resolution (left to right).

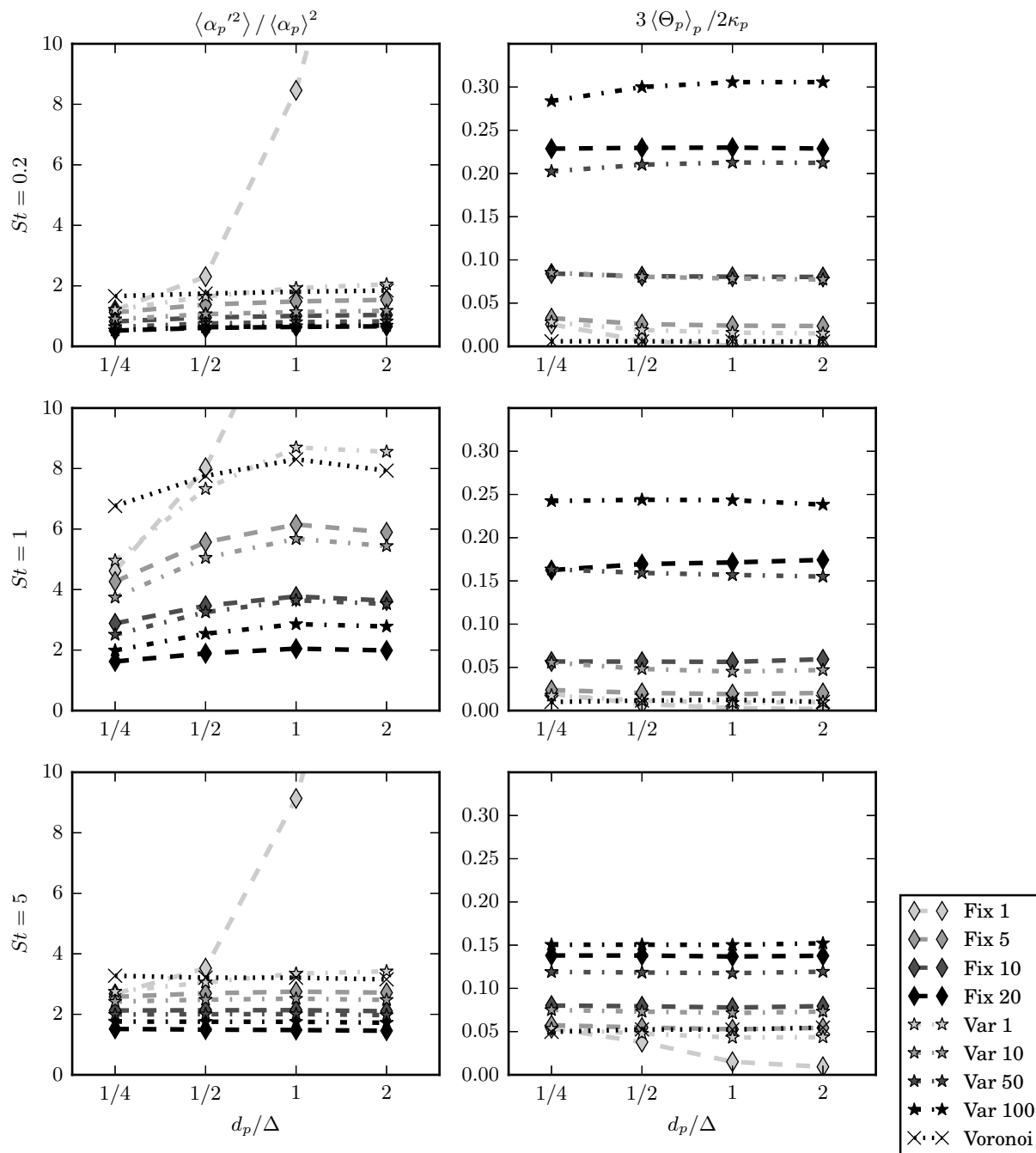


Figure 6: Volume-fraction variance (left) and granular temperature (right) from HIT simulations for three  $St$  particles (top to bottom). Statistics are captured using the various density estimation techniques shown in the legend. Fix and Var refer to kernel density estimation using fixed filter width and variable filter width, respectively. In the case of Fix, the number following refers to the filter width, in multiples of particle diameter,  $h/d_p$ , and in the case of Var, the number refers to the number of particles sampled,  $\mathcal{N}_p$ .

file

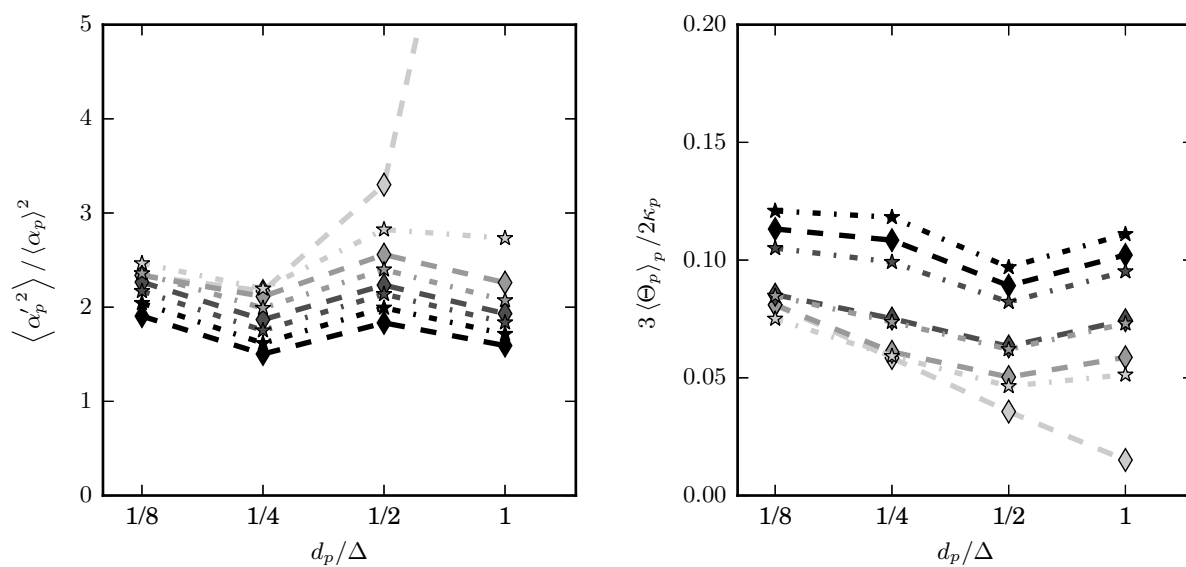


Figure 7: Volume-fraction variance (left) and granular temperature (right) from CIT simulations. The NDF estimation techniques used are the same as those used for the HIT simulations, excluding the Voronoi technique. The legend is shown previously, in Figure 6.

Accepted

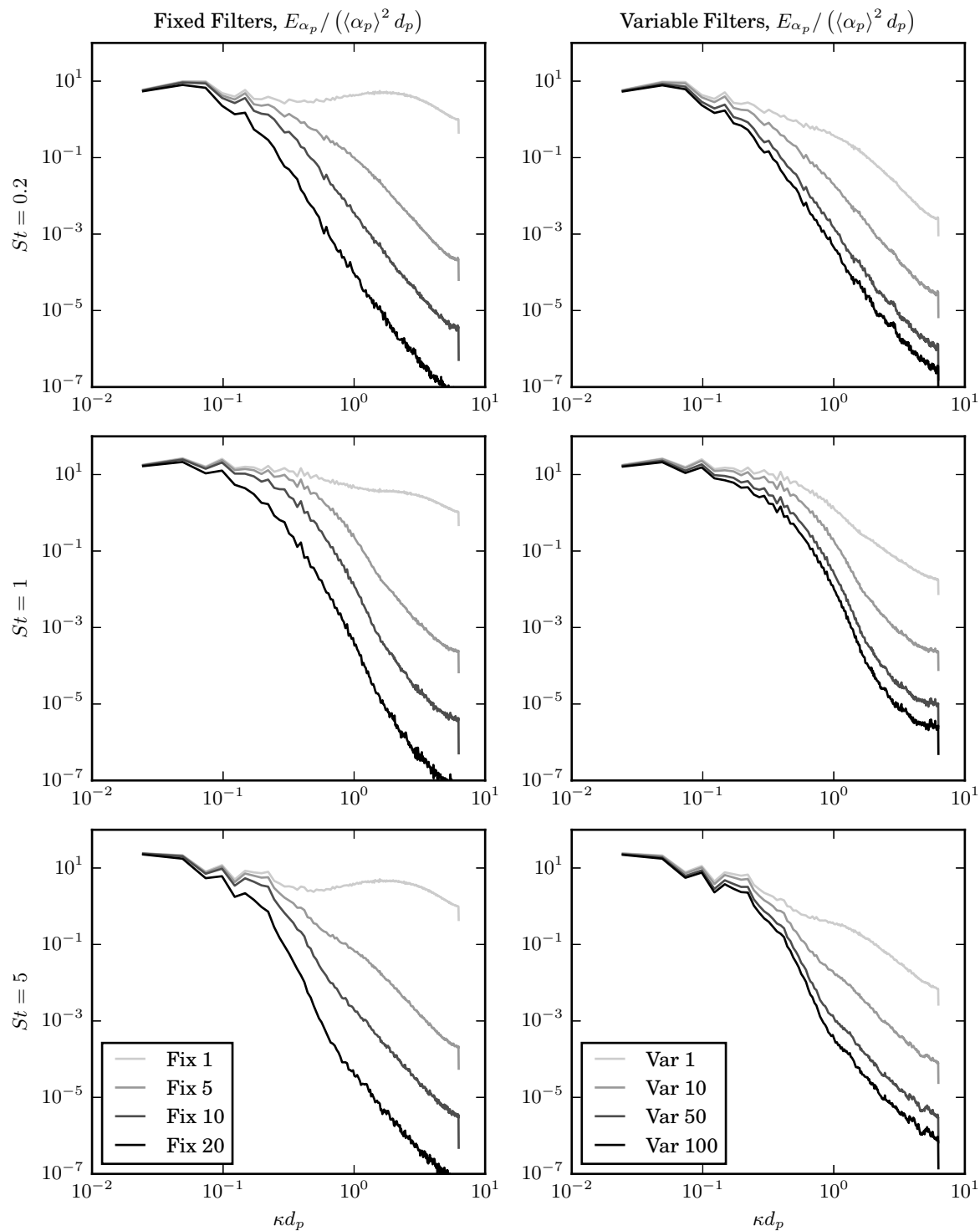


Figure 8:  $\alpha_p$  spectra for EL simulations of HIT at resolution  $d_p/\Delta = 2$  using fixed (left) and variable (right) width filters for the three  $St$  particles (top to bottom).

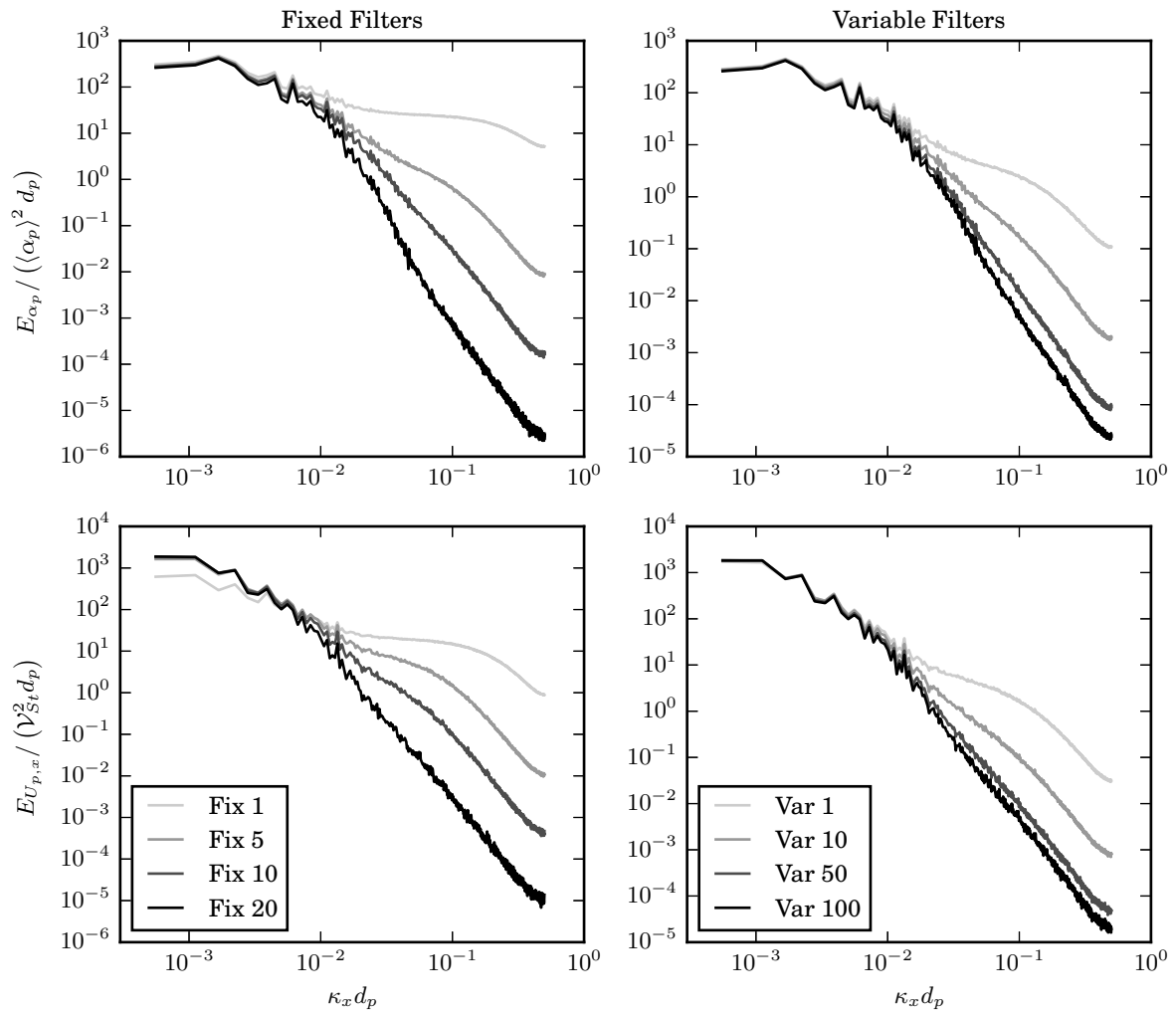


Figure 9:  $\alpha_p$  (top) and  $U_{p,x}$  (bottom) spectra for EL simulations of CIT at resolution  $d_p/\Delta = 1$  using fixed (left) and variable (right) filters.

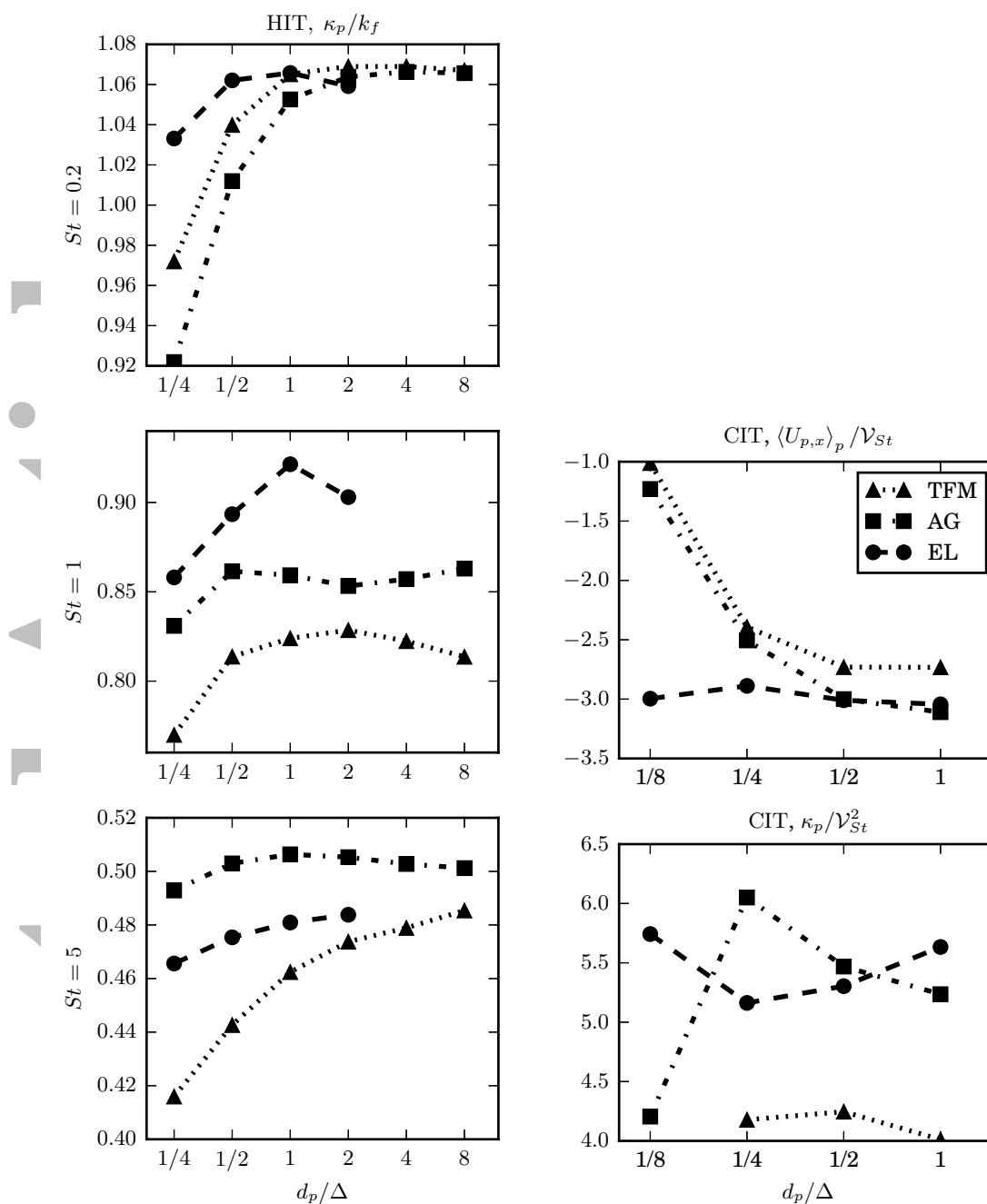


Figure 10: HIT (left) and CIT (right) one-point statistics from the three methods. The total particle fluctuating energy,  $\kappa_p$  is shown for HIT. The particle settling speed,  $\langle U_{p,x} \rangle_p$ , and total particle fluctuating energy are shown for CIT. These statistics do not depend on the EL filter.

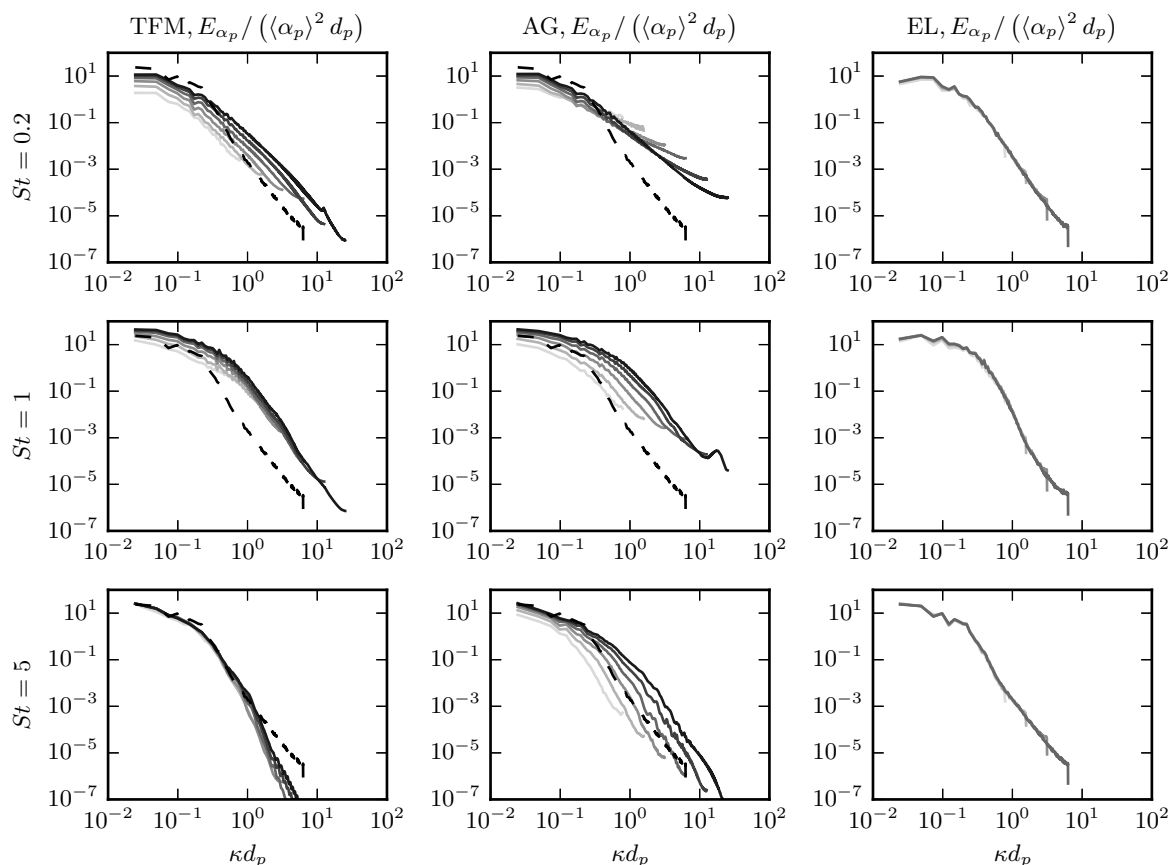


Figure 11:  $\alpha_p$  spectrum from the three methods (left to right) and the three particle Stokes numbers (top to bottom) for HIT case. Spectra are shown for increasing grid resolution. For EL, Fix 10 was used for density estimation. Darker lines refer to higher resolutions. For TFM and AG, the black dashed lines are from the highest resolution EL simulation for comparison.

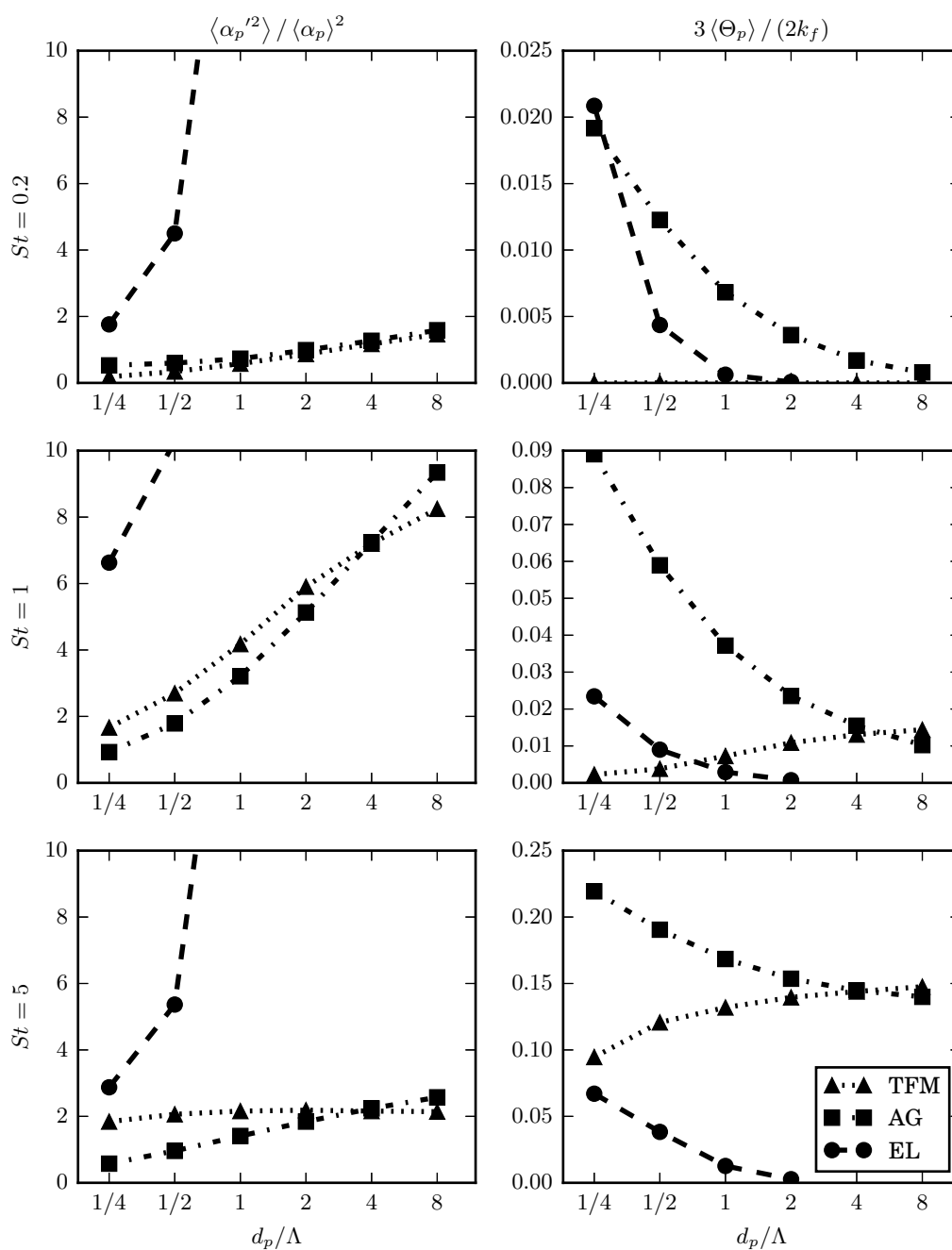


Figure 12: HIT one-point statistics vs. grid resolution for EE methods and filter width for EL method using fixed width filters. Particle volume-fraction variance (left) and granular temperature (right).  $\Delta$  refers to grid resolution,  $\Delta$ , for EE methods and filter width,  $h$ , for EL.



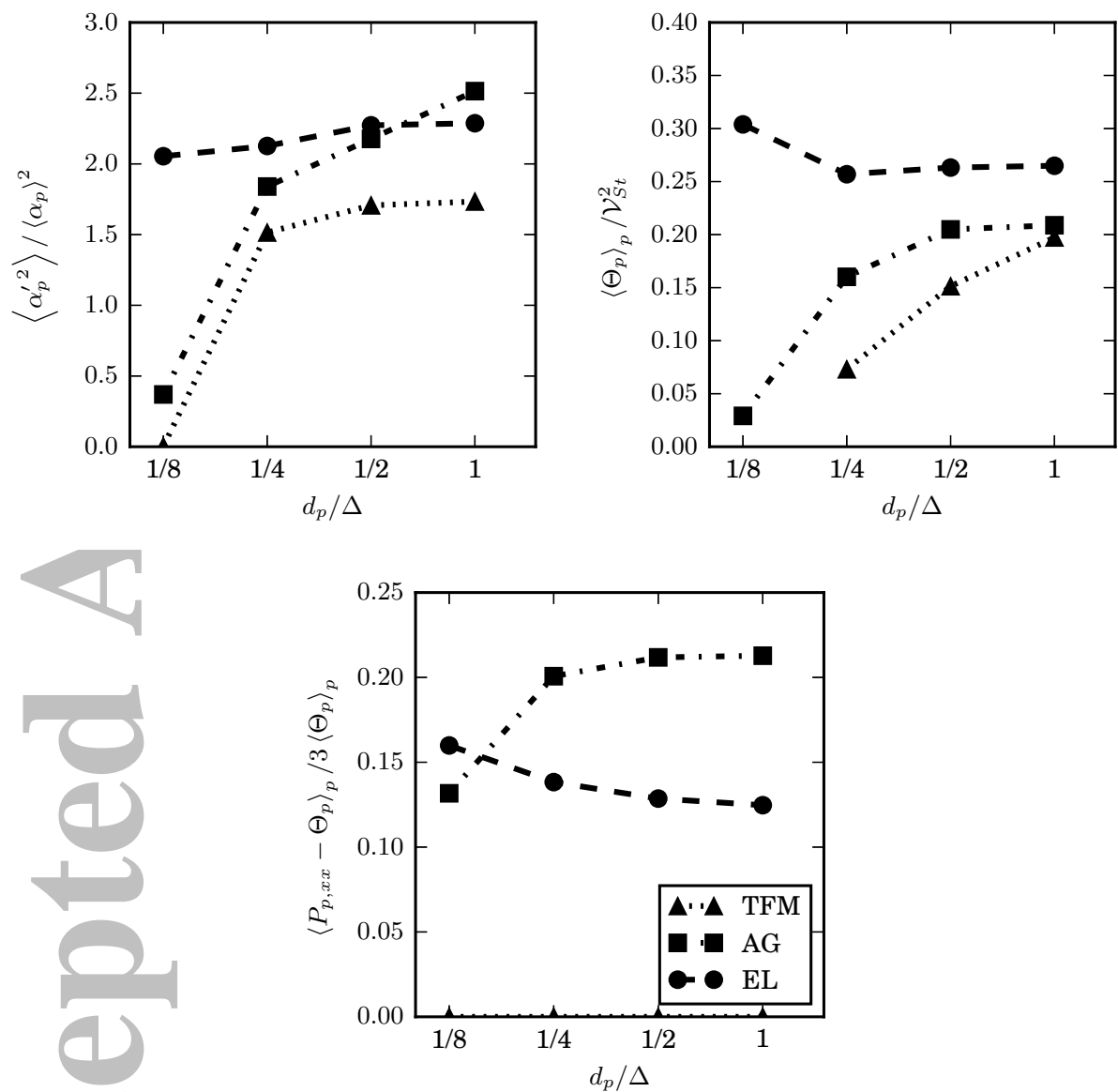


Figure 13: CIT one-point statistics. Volume-fraction variance (top left), granular temperature (top right), and anisotropy in particle pressure tensor (bottom). For EL, Fix 10 was used for density estimation.

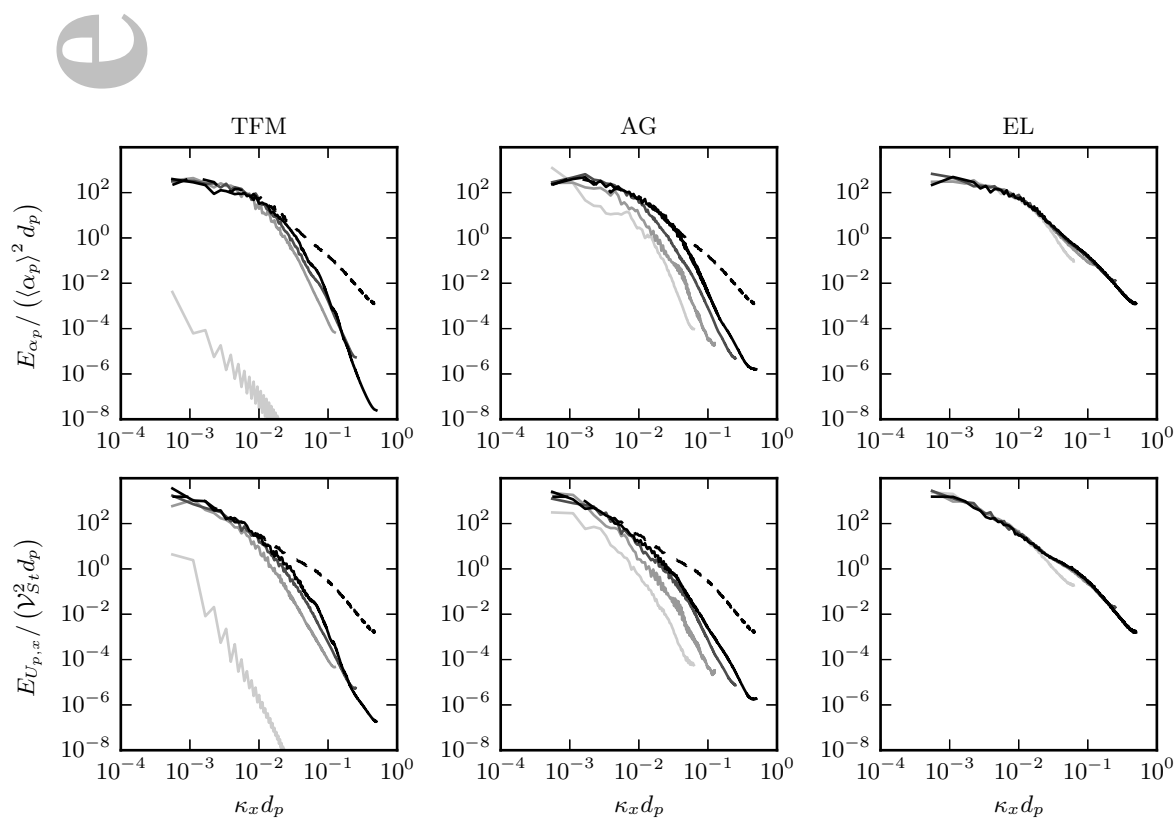


Figure 14:  $\alpha_p$  (top) and  $U_{p,x}$  (bottom) spectra from the three methods (left to right) for CIT case. Spectra are shown for increasing grid resolution. For EL, Fix 10 was used for density estimation. Per row, the black lines are from the highest resolution EL simulation for comparison.

## List of Tables

1	Example kinetic theory coefficients in TFM model for particle phase. . . . .	44
2	Parameters use for HIT simulations. . . . .	45
3	Parameters use for CIT simulations. . . . .	46
4	Statistics from CIT EL simulations with $d_p/\Delta = 1/4$ for different Gaussian volume filtering kernels. . . . .	47

Accepted Article

Table 1: Example kinetic theory coefficients in TFM model for particle phase.

$$\begin{aligned}
 p_{p,c} &= 4\eta\alpha_p g_0 \Theta_p - \nu_{p,b} \nabla \cdot \mathbf{U}_p & \nu_{p,b} &= \frac{8\eta\alpha_p g_0 d_p \sqrt{\Theta_p}}{3\sqrt{\pi}} \\
 \nu_{p,k} &= \frac{1}{2}\Theta_p \left[ \frac{1}{\tau_p} + \frac{\eta(2-\eta)}{\tau_c} \right]^{-1} \left[ 1 + \frac{8}{5}\eta(3\eta - 2)\alpha_p g_0 \right] & \nu_{p,c} &= \frac{8\eta\alpha_p g_0}{5} \nu_{p,k} + \frac{3}{5}\nu_{p,b} \\
 k_{p,k} &= \frac{5}{2}\Theta_p \left[ \frac{3}{\tau_p} + \frac{4\eta(41-33\eta)}{\tau_c} \right]^{-1} \left[ 1 + \frac{12}{5}\eta^2(4\eta - 3)\alpha_p g_0 \right] & k_{p,c} &= \frac{12\eta\alpha_p g_0}{5} k_{\Theta,k} + \frac{3}{2}\nu_{p,b}
 \end{aligned}$$

Table 2: Parameters use for HIT simulations.

Particle Stokes number	$St$	0.2, 1, 5
Grid resolution	$d_p/\Delta$	$\frac{1}{4}, \frac{1}{2}, 1, 2$

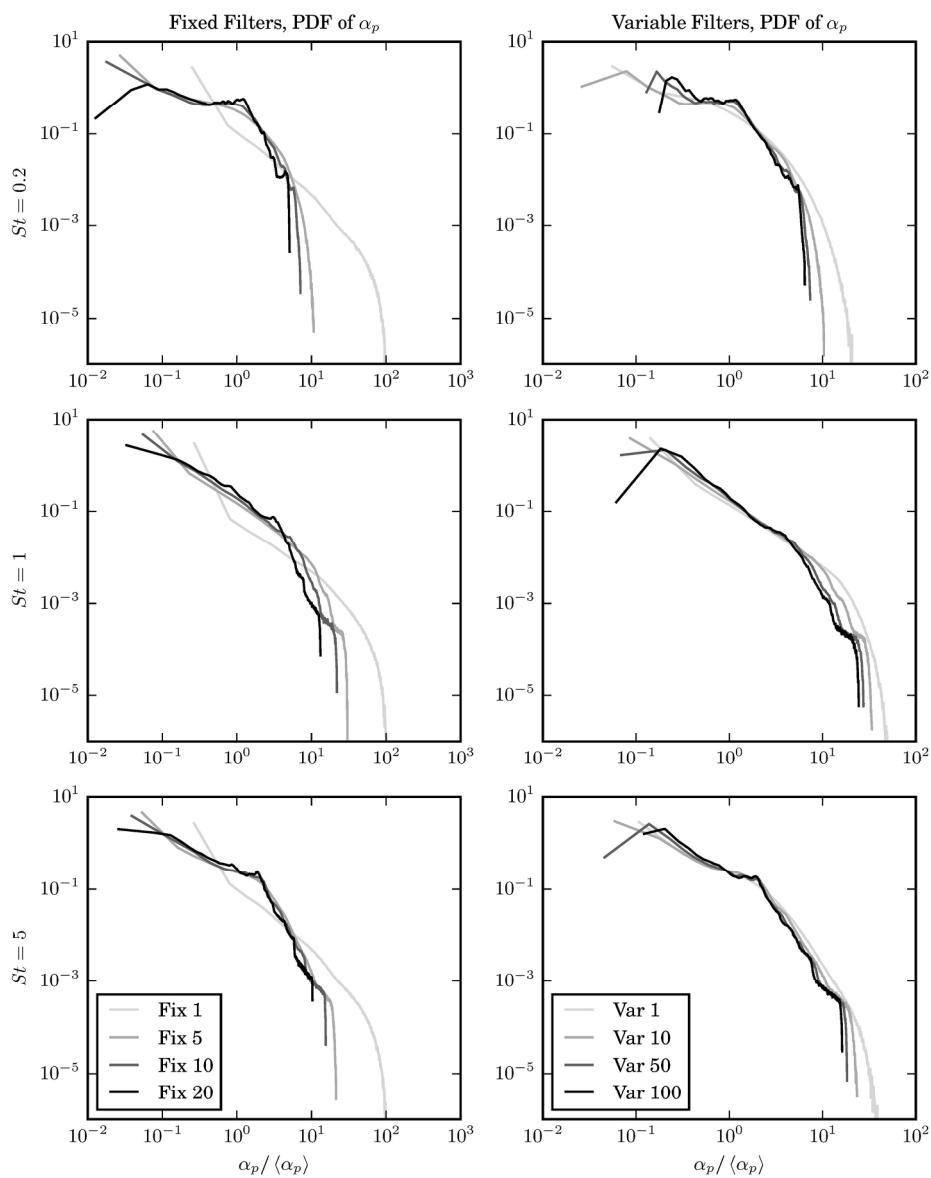
Accepted Article

Table 3: Parameters use for CIT simulations.

Particle diameter	$d_p$	$90 \times 10^{-6} \text{ m}$
Particle density	$\rho_p$	$1000 \text{ kg m}^{-3}$
Fluid density	$\rho_f$	$1 \text{ kg m}^{-3}$
Fluid kinematic viscosity	$\nu_f$	$1.8 \times 10^{-5} \text{ m}^2 \text{ s}^{-1}$
Gravitational acceleration	$g$	$-4.0004 \text{ m s}^{-2}$
Particle Reynolds number	$Re_p$	0.5
Average particle volume fraction	$\langle \alpha_p \rangle$	0.01
Domain size	$\frac{\mathcal{L}_x}{d_p} = 4 \frac{\mathcal{L}_y}{d_p} = 56 \frac{\mathcal{L}_z}{d_p}$	1792
Grid resolution	$d_p/\Delta$	$\frac{1}{8}, \frac{1}{4}, \frac{1}{2}, 1$

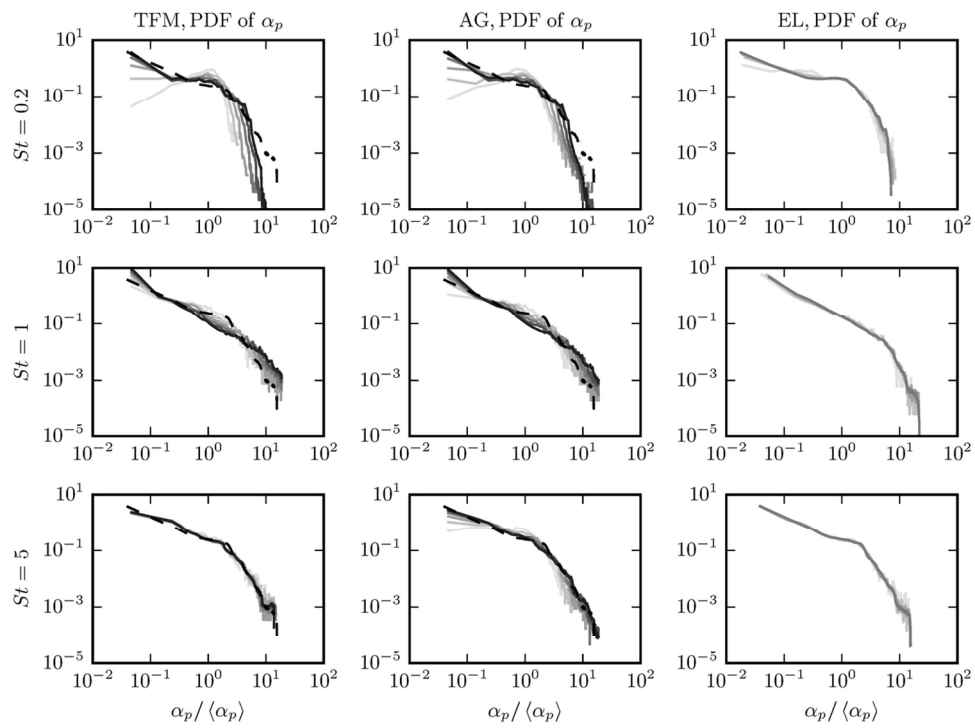
Table 4: Statistics from CIT EL simulations with  $d_p/\Delta = 1/4$  for different Gaussian volume filtering kernels.

$\delta_f/d_p$	$\langle v_{p,x}/V_{St} \rangle$	$\langle v_{p,x}^{\prime 2} \rangle / V_{St}^2$	$\langle v_{p,y}^{\prime 2} \rangle / V_{St}^2$
5	-2.994	6.170	2.735
10	-3.163	7.131	2.970
20	-3.085	5.825	2.512



199x249mm (300 x 300 DPI)





119x89mm (300 x 300 DPI)

Accep